REMOTE SENSING ANALYSIS AND

IMPLICATIONS FOR GROUNDWATER RESOURCES

IN THE KHARGA BASIN, EGYPT

By

SHAWNA PARKS

Bachelor of Arts in Journalism

University of Central Oklahoma

Edmond, Oklahoma

2004

REMOTE SENSING ANALYSIS AND IMPLICATIONS FOR GROUNDWATER

RESOURCES IN THE KHARGA BASIN, EGYPT

Thesis Approved:

Jeffrey M. Byrnes

Thesis Adviser

Mohamed Abdelsalam

Daniel Laó Dávila

ACKNOWLEDGEMENTS

I would like to thank my advisor, Dr. Jeffrey Byrnes, for all of his help, not only with my thesis, but for everything he has done for me throughout my time at OSU. I am also grateful to my committee members, Dr. Mohamed Abdelsalam and Dr. Daniel Laó Dávila, and the Principal Investigator of the Kharga Project, Dr. Estella Atekwana. Cullen Pickens also played an integral role in the remote sensing portion of the Kharga Project.

Name: SHAWNA PARKS

Date of Degree: MAY 2016

Title of Study: REMOTE SENSING ANALYSIS AND IMPLICATIONS FOR
                GROUNDWATER RESOURCES IN THE KHARGA BASIN, EGYPT

Major Field: GEOLOGY

Abstract: Identifying new groundwater resources in Africa is important because climate change may cause the Nile recharge to decrease by the end of the century, affecting water stability in the eleven countries that rely on this river as a water source. Further exacerbating the demand for water in Egypt in particular is a growing population that already lives on a small per capita amount of water. I report results from drainage analysis using a Shuttle Radar Topography Mission (SRTM) digital elevation model (DEM) that corroborate evidence suggesting that the Kharga Basin in Egypt's Western Desert is a closed basin that could have held water in the past. Combined with evidence from other studies, this suggests water from Pleistocene humid periods still resides within the Kharga Basin. Fractures possibly facilitate the vertical movement of this groundwater, consistent with vegetation and tufa deposits following fractures in the basin. Thermal inertia analysis, due to its relation to soil moisture, may help locate areas of relatively shallow groundwater, possibly due to the vertical movement of water along fractures. I report results from remote sensing analysis of optical and thermal images (Moderate Resolution Imaging Spectroradiometer, MODIS) used to create thermal inertia images. Furthermore, I report results from remote sensing analysis of optical (Landsat Operational Land Imager) and radar (Radarsat-1) images and DEMs (SRTM and Advanced Spaceborne Thermal Emission and Reflection Radiometer, ASTER) on the fracture intensity and kinematics in the Kharga Basin. The thermal inertia and fracture density maps were combined with previously published hydraulic conductivity and aquifer thickness maps to perform multi-map analysis and determine the best locations for future water wells. The results suggest the southern end of the major north-south fault is the most conducive to shallow groundwater drilling. For all results, I performed digital image processing and spatial analysis using ENVI and ArcMap.

TABLE OF CONTENTS

LIST OF TABLES

LIST OF FIGURES

CHAPTER I

INTRODUCTION

I.A. Overview

The impact of climate change on hydrologic regimes must be addressed in order to ensure the reliability of water resources in the future. De Wit and Stankiewicz (2006) and Beyene et al. (2010) suggest that Nile drainage extent will decrease by the end of the century affecting water stability in the eleven countries that rely on this river as a water source. Further exacerbating the demand for water in Egypt is a growing population that already lives on a small per capita amount of water. This study was undertaken using spaceborne remote sensing data of the Kharga Basin (Figure 1) within the Nubian Sandstone Aquifer in Egypt in order to highlight areas of potential groundwater development. This study includes the use of Landsat Operational Land Imager (OLI) (NASA 2016a), Radarsat-1 (Canadian Space Agency 2014), and Moderate Resolution Imaging Spectroradiometer (MODIS) (NASA 2016c) images as well as Advanced Spaceborne Thermal Emission and Reflection Radiometer (ASTER) (NASA 2016a) and Shuttle Radar Topography Mission (SRTM) (NASA 2016d) digital elevation models (DEMs). The aim is to produce and analyze fracture, paleodrainage, thermal inertia, and hydraulic conductivity maps. Spaceborne remote sensing is a particularly adept

technique for this location as the problems of inaccessibility and extreme weather

conditions are mitigated by carrying out the study through image processing and analysis.
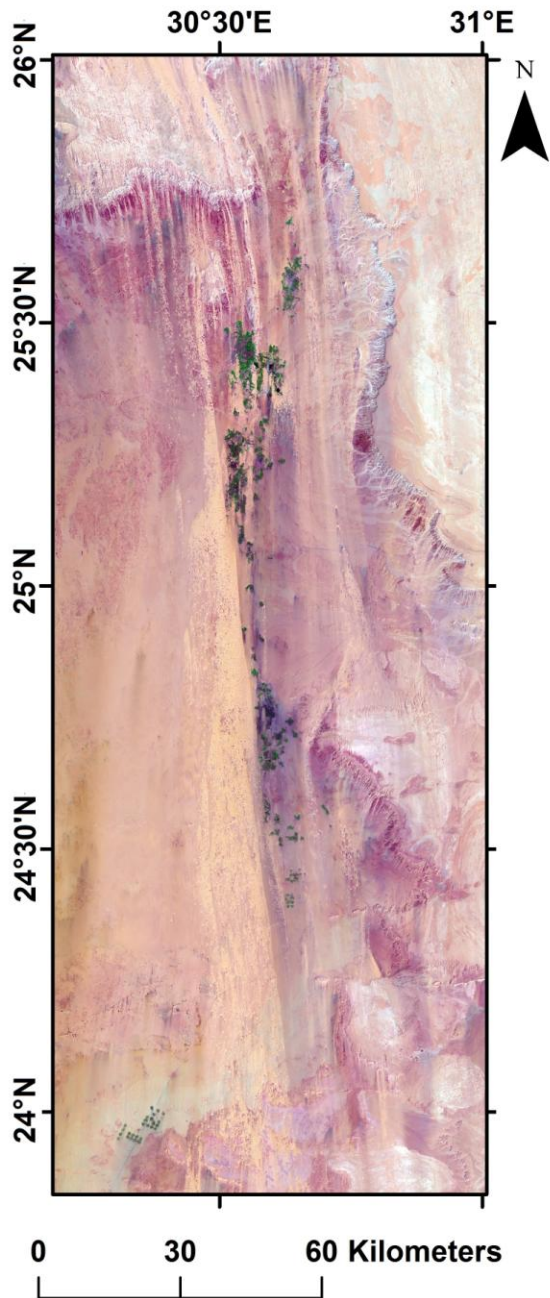
Figure 1: Location of Kharga Basin study area. 7-5-3 RGB Landsat OLI composite

image shows short-wave infrared (R), near infrared (G), and green (B) bands.

The vertical movement of water through fractures could lead to shallower depths of groundwater, making it more economic to extract water in these areas through shallow wells. In the Dakhla Basin (Figure 2), which consists of the same rock formations, Hesse et al. (1987) found that fractures contribute to the rock mass permeability, especially the vertical permeability.
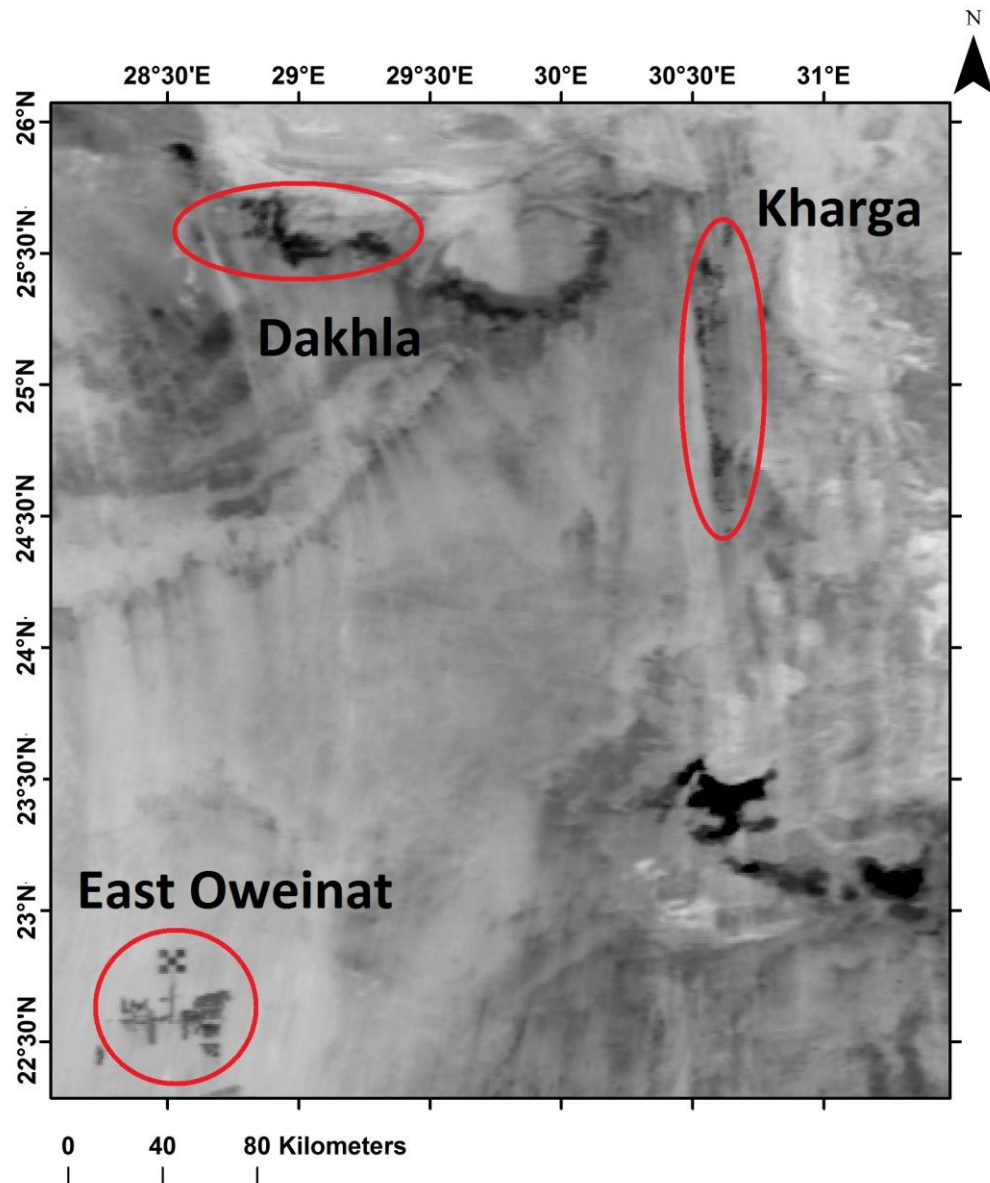
Figure 2: Southern oases of Egypt's Western Desert. Basemap is MODIS albedo image.

The notion that bedrock faults in the Kharga Basin are acting as vertical conduits for groundwater was proposed by Kieniewicz and Smith (2007) based on observation of the proximity of tufa deposits to faults. Hesse et al. (1987) found the mean aperture of joints was 0.59 mm in the north Kharga area. Furthermore, they found that apertures from 0.2-0.5 mm were effective in increasing the permeability through fissure flow in the Dakhla Basin. The work of these researchers resulted in the driving research questions for this project:

- Do fractures in the Kharga Basin allow groundwater to migrate within 10 centimeters depth from the surface?

- Can the areas within the Kharga Basin provide new economic groundwater resources?

I.B. Significance of the Study

The Kharga Basin in Egypt's Western Desert could serve Egypt's water needs by making better use of the Nubian Sandstone Aquifer. The results of this project can be used to determine the best areas for potential groundwater development. This study may be useful in the fields of hydrology, agriculture, pedology, and civil engineering in addition to other geologic studies. The techniques used in this study can be applied not only to other basins in Egypt, but to aquifers around the world. This study produced fracture, paleodrainage, thermal inertia, and hydraulic conductivity maps of the Kharga Basin and will help identify and quantify groundwater resources in Egypt. These maps can guide other researchers to carry out geophysical studies (e.g. magnetic, seismic, electrical resistivity, ground penetrating radar, and gravity surveys) in focused areas

to better understand the subsurface geometry and constrain groundwater models.

I.C. Background of Study Area

The Kharga Basin includes the Kharga Oasis in Egypt's Western Desert, but the basin covers a much larger area than the oasis itself. Figure 3 is a 30 m spatial resolution SRTM density-sliced map showing the elevation of the area.
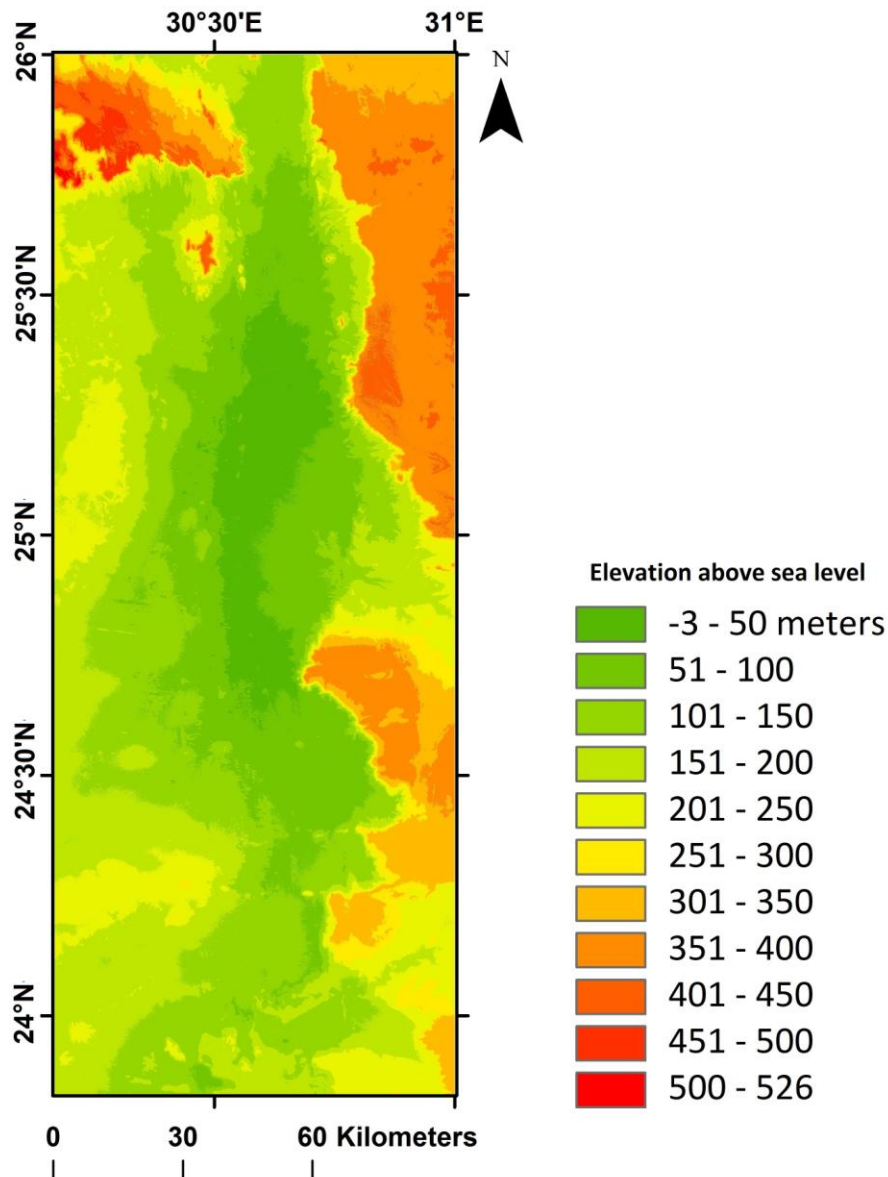
Figure 3: SRTM DEM of the Kharga Basin.

I.D. Geology

Said (1990) and Hermina (1990) give detailed descriptions of the geomorphology and geology of the Kharga area, which are summarized here. The Kharga Basin lies within the Arba'in Desert, which is a subprovince of Egypt's Western Desert. This area is covered by the Nubia Formation sandstones. The Jurassic through Campanian sandstones are interbedded with shales, clays, and sandy clays. Conglomeratic sandstones also occur in the far southern portion of the basin. This facies is mostly continental but does have some shallow marine invasions. The youngest Nubia formation, the Quseir, covers much of the study area, and its vertical succession shows a gradual change from a terrestrial environment to a prodeltaic shallow shelf. Stratigraphic columns of the Nubia Formations in the study area, after Hermina (1990), are shown in Figure 4.
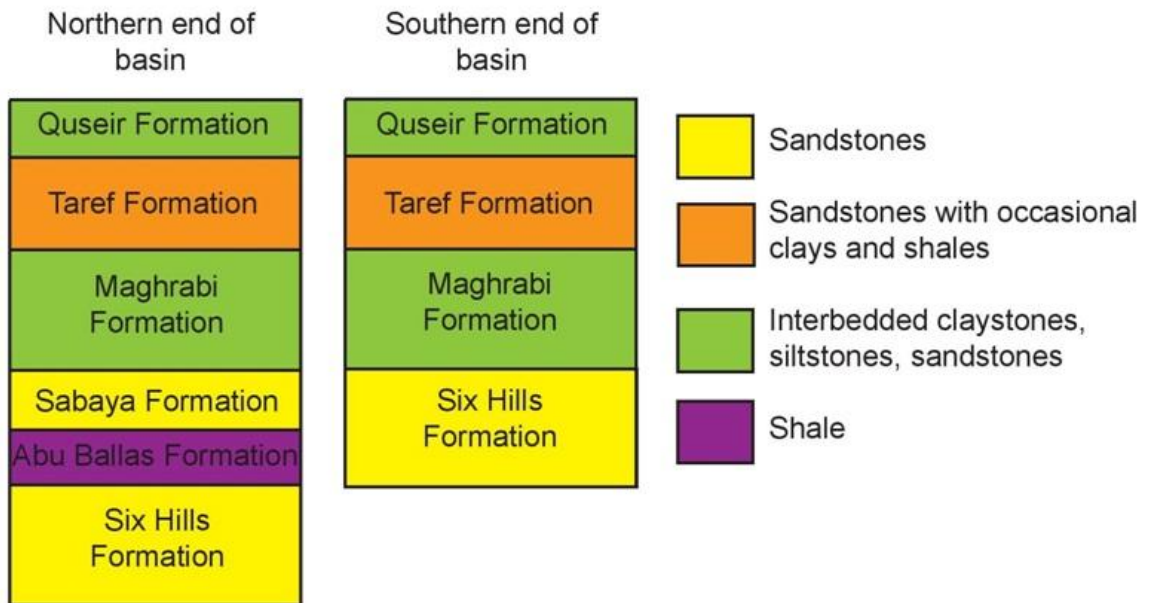
Figure 4. Stratigraphic columns of the Nubia Formations. After Hermina (1990).

A Campanian to Eocene open marine transgressive to regressive facies is seen in the surrounding plateau to the north and east of the basin and consists of thin sandstones, conglomerates, and claystones topped with thick sections of marl, coquina, and limestone. The Jurassic to Eocene sedimentary cover overlies Precambrian crystalline basement. The Nubia formations reach a maximum thickness of about 900 m (Senosy et al. 2013) in the northern part of the basin although many researchers have varying opinions on its thickness. Quaternary deposits are found throughout the study area. Desert pavement creates a mostly hard surface in this region although there is a large dune belt on the western side of the basin. The basin is 220 km long north-south and 15-80 km wide (Kropelin 1993). Most fractures seen at the surface are indicative of Precambrian basement movement with the upper structural level deformation controlled by the thickness and type of the sedimentary cover. Therefore, more fractures are visible in areas of thin sedimentary cover such as in the southern portion of the basin where the thickness is only 500 m. The southern end of the basin is characterized by east-west trending fractures whereas north-south trending fractures dominate in the northern part.

The origin of the depression is not fully understood and may be the result of a combination of factors. Salt weathering combined with wind erosion is one suggestion for the scouring of the basin. If a small depression initially existed, the collection of water in this area could have led to salt weathering with each pluvial episode and the subsequent erosion of this material by wind in interpluvial periods (Haynes 1982). Another suggestion is groundwater sapping processes and fluvial action were the cause of the depressions (Luo et al. 1997). Luo et al. (1997) created a computer simulation to model whether these suggested processes could have occurred rapidly during pluvial

periods. They indicate that during humid periods karstification would dominate. Then, as the climate begins to become less humid, fluvial processes replace karstification. Later, as the climate becomes arid, aeolian processes take over. Furthermore, they suggest the large north-south fault in the center of the basin is most likely what initiated the formation of the depression.

1.E. Tectonics

The tectonic summary given here is based mostly on information by Morgan (1990) and Meshref (1990). Historically there has been some discrepancy as to what extent the Sahara is underlain by cratonic lithosphere. Currently, the Saharan area is considered by some to be an Archean-Paleoproterozoic metacraton that was remobilized during the Neoproterozoic due to collision, leading to events responsible for the heterogeneous crust west of the Nile (Abdelsalam et al. 2002). During the Neoproterozoic/early Cambrian, Pan-African island arc accretion in the present day Red Sea Hills east of the Nile led to the formation of an orogenic belt that was eroded and deposited in the Paleozoic. No major tectonic activity occurred in this area in the Paleozoic. Plate movement took the area to its most southerly latitude of 70°S in the Ordovician, and the continent has been drifting north ever since. In the Mesozoic, Laurasia rifted from Gondwana separating present day Turkey and Egypt, and this event is the cause of initial east-west trending fractures in the area that were later reactivated. Also during this time, differential block movement led to uplift in Egypt causing a drainage shift from south-flowing to north-flowing. A late Mesozoic sea level high resulted in flooding of the area and a switch from a continental to a marine depositional

environment. Sea level fall in the Eocene resulted in continental deposition once again. Most faults in the study area were active after the Lower Eocene (Hermina 1990). In the Oligocene-Miocene, Red Sea rifting and uplift at its margins created the ancestral Nile, and this event is the cause of the NNW-SSE fractures seen in limestones in the Western Desert (Tewksbury et al. 2013). The study area saw no major tectonic activity during the Quaternary (Abdel Zaher et al. 2014). Faults in the study area are normal in nature, with some of the east-west faults exhibiting a strike-slip component of movement as well (Hermina 1990).

1.F. Objectives

There were five main objectives for this study, as follows:

- Map paleodrainage to determine whether Kharga is a closed basin that could have held water in the past.

- Map fractures based on optical and radar images as well as DEMs, determine fracture density, and compare results with previous work.

- Map the geology and hydraulic conductivity and use aquifer thickness maps from previous studies (e.g. Senosy et al. 2013) to determine areas of potentially higher transmissivity.

- Analyze thermal inertia to determine whether fractures serve as conduits to bring groundwater to the surface or very shallow subsurface.

- Use multi-map analysis to determine best areas for potential groundwater resource development based on fracture density, hydraulic conductivity, aquifer thickness, and thermal inertia.

Examining these five objectives required implementation of a variety of remote sensing techniques and data types. In combination they provide a detailed remote sensing analysis of the study area.

1.G. Integration of Remote Sensing Data

The overarching objective of this project was to delineate at least one region for high potential of shallow groundwater resources in the Kharga Basin. This goal is achieved through a multi-map analysis incorporating all of the data necessary to make this recommendation. The four hypotheses relating to the fracture, thermal inertia, paleodrainage, and hydraulic conductivity maps are summarized in Table 1, and each type of remote sensing data is discussed as to how it will help evaluate these hypotheses.

Table 1. Integration of remote sensing data.

Hypotheses / Data type	Identifying fractures and assessing fracture density will highlight areas of shallower groundwater.	Soil moisture will be negligible in most areas, but increased moisture near fractures may indicate vertical groundwater movement.	Mapping paleodrainage will corroborate evidence that Kharga is a closed basin that could have held water in past humid periods.	Mapping hydraulic conductivity will result in the discovery of areas with potentially higher transmissivity.
Visible and near infrared (VNIR) and short wave infrared (SWIR) remote sensing bands (Landsat OLI)	Pan-sharpened Landsat images used with directional filters to map fractures and areas of fracture density.	Apparent thermal inertia used to determine soil moisture. These bands were used to determine albedo, one component in calculating apparent thermal inertia.		Landsat images used with high-pass and Sobel filters to map geologic boundaries, which were subsequently related to hydraulic conductivity.
Thermal infrared (TIR) remote sensing bands (ASTER, Landsat OLI)		TIR bands used to determine day-night temperature difference, which was also used in calculating apparent thermal inertia.		
Radar remote sensing bands and DEMs (Radarsat-1, SRTM, and ASTER)	Radarsat data and ASTER- and SRTM-derived DEMs used to map fractures on the surface and, with Radarsat, up to two meters in the subsurface (Abdelsalam et al. 2000).		SRTM DEM data used in the ArcMap Arc Hydro tool to create a paleodrainage map.	SRTM DEMs used to map geologic boundaries.

CHAPTER II

REVIEW OF LITERATURE

II.A. The Nubian Sandstone Aquifer (NSA)

The Nubian Sandstone Aquifer (NSA) underlies parts of Egypt, Chad, Libya, and Sudan. One conservative estimate of the water available in this aquifer is 28,000 km^3 (Ebraheem et al. 2002). Some regional recharge does occur, but it is of little significance to the overall groundwater volume (Heinl and Brinkmann 1989; Thorweihe 1990). Many studies have shown that the bulk of the NSA groundwater recharge came from the last five pluvial episodes of the Pleistocene and Holocene (Abell and Hoelzmann 2000; Hoelzmann et al. 2000; Pachur and Hoelzmann 2000, Smith et al. 2004a; 2004b, 2007; Kieniewicz and Smith 2007, 2009). These pluvial episodes relate to interglacial stages that have been dated as follows: 320-250, 240-190, 155-120, 90-65, and 10-5 ka (Szabo et al. 1995). Due to interbedding of clays, the aquifer in the Kharga Basin is semiconfined, although this is not the case for the entire NSA (Ebraheem et al. 2003).

The economic pumping depth in the Kharga Oasis is as shallow as 38 m (Ebraheem et al. 2003). The depth to Precambrian crystalline basement is variable throughout the basin. Multiple studies have shown that extraction of water from the NSA in Egypt is groundwater mining as the aquifer has not been in a steady state for thousands

of years (Heinl and Brinkmann 1989; Ebraheem et al. 2002, 2003, 2004; Gossel et al. 2004; Robinson et al. 2007). Therefore, more studies are needed to assess the feasibility of current groundwater pumping projects and the availability of future groundwater resources. Based on present knowledge, current irrigation projects in East Oweinat (Figure 2) will result in a significant groundwater cone of depression that will affect the Kharga Oasis within 100 years (Ebraheem et al. 2002, 2003). A recent study calculates the difference in hydraulic head between the northeast and southeast portions of the basin will be 140 m by 2060, with the severe deepening of groundwater table occurring in the northeastern portion of the basin (Mahmod et al. 2013).

II.B. Geochemistry

Geochemical studies of the area focus on age dating of lacustrine and groundwater precipitated sediments in order to constrain the dates of pluvial episodes across the eastern Sahara as well as isotopic studies of shells and sediments in attempt to establish the source of these waters. Tufas found along the escarpment bordering the eastern side of the Kharga Basin that have been dated with U-series isotopic systematics and the dates fall within or very near the Pleistocene pluvial episodes suggested by Szabo et al. (1995) (Smith et al., 2004a, 2004b, 2007). [14]C dating of lacustrine carbonates by Pachur and Hoelzman (2000) is in line with the dates of the Holocene pluvial episode. In some cases, archeological artifacts can also be used to verify dates obtained through U-series dating as the pluvial episodes occurred in conjunction with human occupation (Smith et al. 2004b). In addition, authigenic calcite silts and gastropod shells from the same area show $\delta^{18}O$ values suggesting some input of an isotopically heavier water

source than the Atlantic indicating that groundwater in the area is of multiple origins. This isotopically heavier water source that provides a portion of the groundwater is most likely monsoons from the Indian Ocean but possibly the Mediterranean as well (Kieniewicz and Smith 2007). In the most recent wet phase, it is possible the annual precipitation reached 900 mm per year. This rate is based on an estimate of the size of the West Nubian Paleolake calculated from lake carbonate ground coverage, Global Positioning System (GPS) data, and the estimation of the necessary precipitation required to sustain a lake of that size (Hoelzmann et al. 2000). Radiocarbon dating and isotope analysis of the groundwater itself corroborate the evidence of a recent Holocene wet period and several older wet periods. In addition, these methods have shown that no water within the NSA is from recent groundwater recharge (Thorweihe 1990). Analysis of groundwater samples in the Kharga Basin suggests the presence of Na_2SO_4 and $NaHCO_3$ enriched groundwater (Boulos 1990).

II.C. Paleodrainage and Lineament Analysis

The majority of remote sensing studies in the eastern Sahara focus on paleorivers and paleolakes. Radar data unveils the multitude of drainage channels lying beneath the sand (e.g. McCauley et al. 1982). Studies showing evidence of large paleolakes in the area from remote sensing images include: Pachur and Rottinger (1997), Ghoneim and El-Baz (2007), Maxwell et al. (2010), and Khan et al. (2014). Another study discovered evidence that suggests a possible Miocene age river in Libya that would have rivaled the modern-day Nile in length (Paillou et al. 2009). Drainage networks along the escarpment surrounding the Kharga Basin have been analyzed with the Satellite Pour l'Observation

de la Terre (SPOT) data to study groundwater sapping processes that may have created the depression (Luo et al. 1997). Abdelsalam et al. (2008) used Landsat Thematic Mapper (TM), ASTER, and SRTM data to determine the temporal evolution and future loss of the present-day Tushka lakes that appeared in 1998 and are now in decline. Bastawesy et al. (2008) used ASTER and SPOT data to determine that the water loss from the lakes was mostly due to evaporation rather than seepage to recharge the underlying aquifer.

There are two key studies that use remote sensing to analyze faults and fractures, or lineaments, in the region. Robinson (2002) used Shuttle Imaging Radar – Phase C (SIR-C), Radarsat, and topographic data to map faults and paleochannels concluding that the area between the Selima Sand Sheet and the Kharga Basin contains a fractured-rock aquifer. Abdel Zaher et al. (2014) used Landsat Enhanced Thematic Mapper Plus (ETM+) and SRTM data to create a lineament map taking into consideration drainage maps and Bouguer gravity anomaly maps. This study did not combine all the data into one comprehensive lineament map nor did it use Radar data. Hesse et al. (1987) carried out a field investigation of fractures in the exposed outcrops. Despite these previous studies, no fracture density maps for the Kharga Basin have been previously published. Hence, there is a need for fracture density analysis because of its importance in understanding groundwater potential due to fracture contribution to enhancing secondary porosity and permeability as well as weathering that increases areas of water storage (Anudu et al. 2011).

II.D. Thermal Inertia

Thermal inertia is a measurement of a material's resistance to change in temperate, and thermal inertia models for remote sensing have been a matter of discussion since the 1970s. Initially, they were of interest for geologic mapping based on thermal properties of rocks in cases where alteration at the surface made identification difficult (Kahle 1977). Gillespie and Kahle (1977) give a detailed overview of how these early thermal inertia images were created. Diurnal temperature difference and albedo have always been the basis of thermal inertia models, with ground measured variables and various scaling factors accounting for the differences among them. Pratt and Ellyett (1979) showed the relationship between thermal inertia of soils and their composition, porosity, and moisture content for the purpose of remote sensing studies of soils. They concluded remote application of thermal inertia models to interpret variable soil moisture was feasible with some knowledge of the soil type and porosity. Price (1985) noted that areas of vegetation caused errors in remotely sensed thermal inertia estimation due to surface evaporation. This problem was rectified by Xue and Cracknell's (1995) thermal inertia model. By using a second degree polynomial of the linearized boundary condition, they were able to create a model that was accurate for surface temperatures between 280 and 310 K and in regions covered by vegetation. Furthermore, their model measured real thermal inertia as opposed to the apparent thermal inertia measured by previous models. Cai et al. (2007) used the Xue and Cracknell (1995) model to relate thermal inertia measured in the Northern China Plain to soil moisture based on Ma and Xue's (1990) look-up tables. They compared this data with in-situ measurements and found the average difference of the results were within 4.32%. Scheidt et al. (2010) used the same thermal inertia model and soil moisture look-up tables in their study of the

White Sands Dune Field, New Mexico. They advanced the analysis further to determine the potential for soil erosion based on the soil moisture values.

CHAPTER III

METHODOLOGY

III.A. Paleodrainage

To determine the paleodrainage, 30 m and 90 m spatial resolution SRTM DEMs were used. Results from the two were compared, and ultimately the 30 m spatial resolution DEM was used for the final product. The Arc Hydro tools within ArcMap were used to create the paleodrainage map. These tools enable the user to carry out extensive hydrologic analysis including: evaluate sinks, determine flow direction and accumulation, define streams and their segmentation, and process drainage lines and catchment areas. For each step in the process, ESRI tutorials were used (e.g. Djokic 2008; ESRI 2011; ESRI 2013).

The area was modeled as a combined dendritic and deranged drainage network with unknown sink and stream locations because there are no modern day streams to use as controls and to account for potential sub-basins. Two steps within the process required an iterative approach: sink selection and stream definition. The final sink selection was determined by those which resulted in drainage lines that were most geologically feasible. Sink selection can be determined through minimum depth, volume, area,

drainage area, or any combination thereof. The final sink selection was a combination of depth and area. Depths less than 16 m were not selected as sinks because this is the margin of error of SRTM data (U.S. Department of the Interior 2008). Of those sinks deeper than 16 m, the six with the largest area were selected for the final product. For the stream definition component, Arc Hydro recommends a stream definition that is at least 1% of total accumulation; however, this resulted in a very sparse drainage network. By significantly decreasing the required accumulation needed for a defined stream, the modeled drainage lines matched those that can be visually interpreted along the plateau and take into account lower order streams throughout the study area (Figure 5).
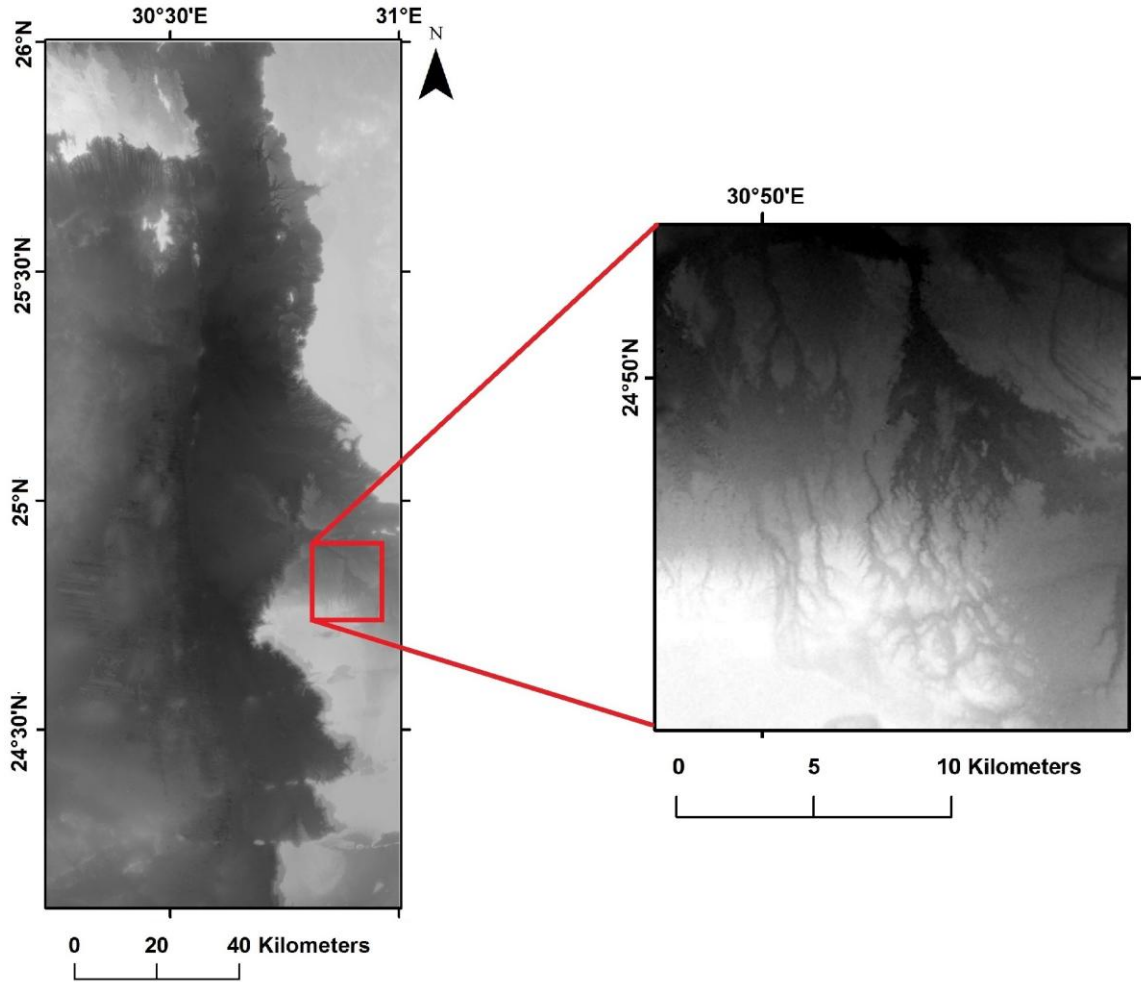
Figure 5: Paleochannels on the plateau. Data is 30 m spatial resolution SRTM DEM.

III.B. Lithology and Hydraulic Conductivity

To assess the hydraulic conductivity, the lithology must first be determined.

Multiple geologic and hydraulic conductivity maps from previous studies were used. The

basis for the geologic map created in this study was a formation map from Hermina

(1990). The descriptions of the formations were used to create a lithology map. The

geological contacts between different formations were mostly determined through visual

inspection of Landsat OLI images and SRTM DEMs in ArcMap. Landsat OLI images

with high-pass and Sobel filters were used in RGB combinations of: 7-5-3, 6-4-2, and 7-4-2. The 7-5-3 (equivalent of 7-4-2 for Landsat Thematic Mapper (TM) bands) combination is good for desert regions. The 6-4-2 combination (equivalent of 5-3-1 for Landsat TM bands) highlights differences in the texture of the topography, and 7-4-2 (equivalent of 7-3-1 for Landsat TM bands) can help distinguish rock types (Quinn 2001). In cases where sand cover obscured geological contacts, they were modeled after Hermina (1990). After the geologic map was created, this was compared with previous hydraulic conductivity maps (e.g. Hesse et al. 1987; Thorweihe 1990; Ebraheem et al. 2002). Hydraulic conductivity data from formations in the Dakhla Basin (e.g. Hesse et al. 1987) was extrapolated into some of those same formations in this study.

III.C. Thermal Inertia

III.C.1. Thermal Inertia Modeling

Thermal inertia (TI) is a measurement of a material's resistance to change in temperature. Higher TIs represent smaller changes in temperature while lower TIs represent larger changes in temperature. The following equation defines thermal inertia (*P*).

$$P = \sqrt{K\rho c} \qquad (1)$$

K is thermal conductivity, ρ is density, and *c* is specific heat. While these variables cannot be determined through remote sensing methods, apparent thermal inertia (ATI) can be. ATI is defined in the following equation.

$$ATI = \frac{1 - A}{\Delta T} \qquad (2)$$

A is albedo and ΔT is the difference between maximum and minimum land surface

temperature (LST). Scheidt et al. (2010) scaled the ΔT for their ASTER data as follows.

$$\Delta T = T_{max} - T_{min} \qquad (3)$$

$$T_{max} = T_1 + \frac{(T_1 - T_2)[\cos(\omega t_{max}) - \cos(\omega t_1)]}{\cos(\omega t_1) - \cos(\omega t_2)} \qquad (4)$$

$$T_{min} = T_2 + \frac{(T_1 - T_2)[\cos(\omega t_{min}) - \cos(\omega t_2)]}{\cos(\omega t_1) - \cos(\omega t_2)} \qquad (5)$$

T_1 = daytime satellite temperature; pixel value scaled X 0.02 per product specifications

(K)

T_2 = nighttime satellite temperature; pixel value scaled X 0.02 per product specifications

(K)

t_{max} = time of maximum air temperature, determined from a local weather station

(seconds)

t_{min} = time of minimum air temperature, determined from a local weather station

(seconds)

t_1 = time of daytime satellite LST acquisition (seconds)

t_2 = time of nighttime satellite LST acquisition (seconds)

ω = Earth's angular frequency, 7.27 x 10^{-5} rad/s

     This study created TI images with both scaled and non-scaled temperature data to

determine which was more suited to the Moderate Resolution Imaging Spectroradiometer

(MODIS) data. While the non-scaled ASTER temperature data resulted in underestimation of TI in the Scheidt et al. (2010) study, that did not appear to be the case with the MODIS data in this study. Therefore, the results shown here do not have this temperature scaling applied.

By using Xue and Cracknell's (1995) thermal inertia model, actual thermal inertia can be derived from the ATI and several variables including the phase difference of the satellite recorded maximum and minimum temperatures from the actual maximum and minimum temperatures. The equation is as follows.

$$P = \frac{(1-A)S_0 C_t}{\Delta T \sqrt{\omega}} \left\{ \frac{A_1\left[\cos(\omega t_2 - \delta_1) - \cos(\omega t_1 - \delta_1)\right]}{\sqrt{1 + \frac{1}{b} + \frac{1}{2b^2}}} + \frac{A_2\left[\cos(\omega t_2 - \delta_2) - \cos(\omega t_1 - \delta_2)\right]}{\sqrt{2 + \frac{\sqrt{2}}{b} + \frac{1}{2b^2}}} \right\} \tag{6}$$

$$A_1 = \frac{2}{\pi}\sin\delta\sin\alpha + \frac{1}{2\pi}\cos\delta\cos\alpha\left[\sin(2\Psi) + 2\Psi\right] \tag{7}$$

$$A_n = \frac{2\sin\delta\sin\alpha}{n\pi}\sin(n\Psi) + \frac{2\cos\delta\cos\alpha}{\pi(n^2-1)}\left[n\sin(n\Psi)\cos\Psi - \cos(n\Psi)\sin\Psi\right] \tag{8}$$

$$b = \frac{\tan(\omega t_{max})}{1 - \tan(\omega t_{max})} \tag{9}$$

$$\delta_1 = \arctan\left(\frac{b}{1+b}\right) \tag{10}$$

$$\delta_2 = \arctan\frac{b\sqrt{2}}{1 + b\sqrt{2}} \tag{11}$$

$$\Psi = \arccos(\tan\delta\tan\alpha) \tag{12}$$

A = albedo from standard albedo product; pixel value scaled X 0.001 per product specifications (no units)

S_0 = solar constant, 1367 W/m^2

23

C_t = atmospheric transmittance, 0.72-0.74 (no units), (see Appendix A for how it was calculated)

ω = Earth's angular frequency, 7.27 x 10^{-5} rad/s

$\Delta T = T_{max} - T_{min}$

α = latitude, 24° (converted into radians)

δ = solar declination (converted into radians); determined using calculator at

http://www.esrl.noaa.gov/gmd/grad/solcalc

t_1 = time of daytime satellite LST acquisition (seconds)

t_2 = time of nighttime satellite LST acquisition (seconds)

t_{max} = time of maximum air temperature, determined from a local weather station (seconds)

This equation will result in a value with thermal inertia units (TIU) $Jm^{-2}K^{-1}s^{-1/2}$. This model works for areas of variable soil moisture, including arid locales such as the majority of the study area, but also vegetated areas such as that in the Kharga Oasis portion of the basin for temperatures ranging from 280 to 310 K (Xue and Cracknell 1995). All temperature data used in this study falls within this range.

Ultimately, thermal inertia was measured for its relation to soil moisture. An increase in soil moisture has been related to an increase in thermal inertia (Pratt and Ellyett 1979; Ma and Xue 1990; Xue and Cracknell 1995; Cai et al. 2007; Scheidt et al. 2010) (Figure 6). This study tests whether fractures in the area may act as vertical conduits that bring groundwater to the near surface. If they do, the soil moisture, and therefore the thermal inertia, should be higher around fractured areas.
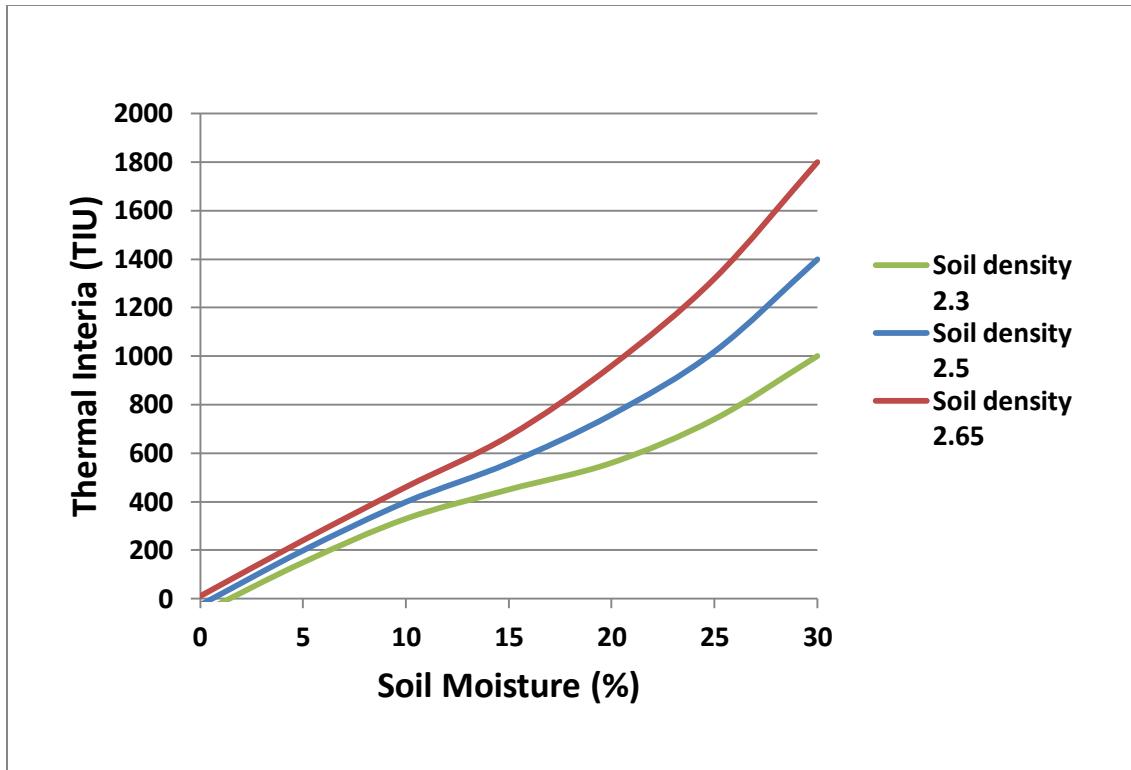
Figure 6: Relationship between soil moisture and thermal inertia. After Scheidt et al. (2010).

Scheidt et al. (2010) assumed a density of 2.65 g/cm^3 for soil for their study in the White Sands Dune Field, New Mexico. This is an appropriate assumption for this study as well due to the similar aeolian system.

III.C.2. Data

MODIS 1 km spatial resolution data were used to investigate thermal inertia. Although ASTER data have a much finer spatial resolution, the timing of the Aqua satellite data acquisition over the study area combined with the spatial crossover between day and night passes has necessitated the use of MODIS data over ASTER. When combined with the other parameters for groundwater potential examined through this research, the 1 km spatial resolution is adequate for the purposes of this study.

III.C.2.a. Lands Surface Temperature

Day and night land surface temperatures (LST) were retrieved from the

MODIS/Aqua Land Surface Temperature/Emissivity 5-Min L2 version 41 standard

product MYD11_L2 through the Reverb ECHO NASA website

(http://reverb.echo.nasa.gov/reverb/). The generalized split-window algorithm used to

create this product (e.g. Wan 1999) has been verified to be accurate within 1°C (Wan et

al. 2004). Later versions of the algorithm, including the one used for this product, have

further improved previous versions. Version 41 specifically addresses the version 5

underestimation of temperature in arid regions (U.S. Department of the Interior 2014).

Version 6 data would be acceptable as well, but this data for the study area only goes up

to 2005. Due to the potential water table changes caused by pumping in the East Oweinat

area (Ebraheem et al. 2002), newer data is more appropriate for this study. For data

covering the study area between 2007 and 2015, there were 181 granules that contained

10% cloud cover or less. Of those 181 granules, there were seven corresponding pairs

that were taken near maximum and minimum daily temperature and within 12 hours of

each other. The data quality of the pairs was inspected as well as the matching albedo

product data for each pair. Two data sets were removed from consideration because of

missing data within the study area. Another data set was removed for its low ΔT values.

The remaining four sets were used for this analysis. The change in temperature from day

to night is important when considering the results of the data. A large ΔT is preferable as

highlighted by Cai et al. (2007) who found that the greater the difference in maximum

and minimum LST, the less change in thermal inertia and therefore less potential error

(Figure 7). Wind speed has also been determined to have a large effect on soil moisture

by affecting land surface heat fluxes (Wetzel et al. 1984; Zhang et al. 2003). The algorithm used for this study works without wind speed as a parameter, but minimizing outside variables is still preferable. This study does assume constant wind speed throughout the day as well as a stable atmosphere similar to the assumptions used in the Xue and Cracknell (1995) study from which the thermal inertia model is based. The ΔT and wind speed are shown in Table 2. Data collected at 11:45 UTC (1:45 p.m. local time) and 23:55 UTC (1:55 a.m. local time) on March 5, 2010 were determined to be the best candidates for soil moisture study. Not only does this data set have the largest variation in daily air temperature, but it also has the slowest recorded wind speeds of all the data sets at the times of satellite acquisition as well as the least variable wind speed throughout the day.
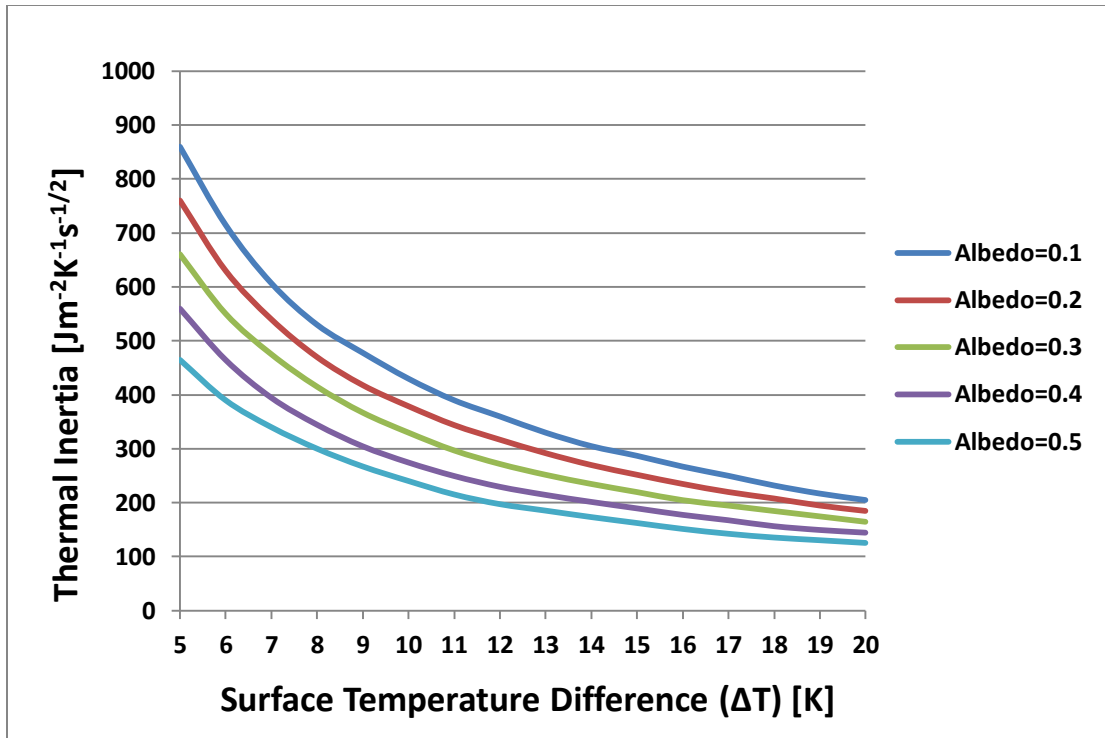
Figure 7: Relationship between surface temperature difference and thermal inertia. After Cai et al. (2007).

Table 2. ΔT and wind speed values for land surface temperature data. Mean difference between day and night temperature (ΔT) values determined from histograms of land surface temperature (LST) data. Wind speed values are from The Weather Channel LLC (2015).

Acquisition Dates	ΔT (K)	Wind speed (km/h)
3/5/2010 and 3/6/2010	33.34	7.6 and 0
3/20/2013 and 3/21/2013	16.39	15.3 and 2.0
4/5/2013 and 4/6/2013	22.89	18.5 and 6.4
6/14/2015 and 6/15/2015	26.43	19.3 and 4.0

III.C.2.b. Albedo

Shortwave broadband white sky albedo was retrieved from MODIS/Terra +Aqua Albedo 16-Day L3 version 5 standard product MCD43B3 through the Reverb ECHO NASA website. This product contains land surface albedos derived from atmospherically-corrected reflectance data obtained from sensors on two satellites and seven bands over a 16 day period. A Bidirectional Reflectance Distribution Function is created from the data and then integrated over all irradiance directions to determine the white sky albedo. Multiple publications have validated the high accuracy of this product (NASA 2014). All of the albedo images used in this study have at least a 98% good quality rating from NASA.

III.C.2.c. Methods

Figure 8 shows the workflow for the thermal inertia mapping.

Step 1
- Albedo and LST images were uploaded into ArcMap.
- The LST images lacked spatial data, and so they were georeferenced to the albedo image and each other. They were warped with a polynomial transformation.

Step 2
- The georeferenced rasters were exported with squared pixels at 1 km spatial resolution.
- Subsets of each image with the same geographic coordinates and same number of samples and lines were created in ENVI.

Step 3
- The Band Math Tool in ENVI was used to create ΔT images and ATI images (using equations 2-3).

Step 4
- Excel was used to create a single coefficient to scale ATI images to TI images (using equations 6-12.)
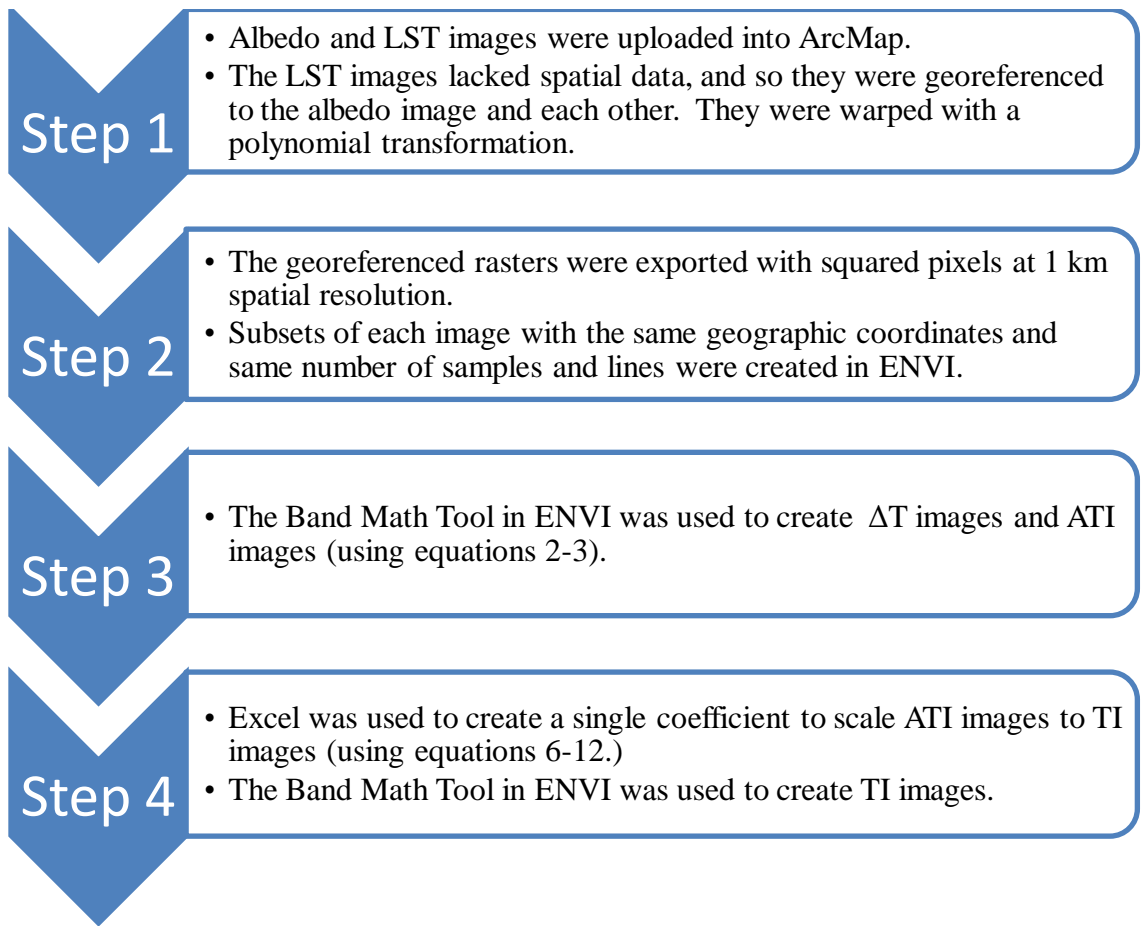- The Band Math Tool in ENVI was used to create TI images.

Figure 8: Thermal inertia workflow.

To ensure that slight georeferencing error would not result in a dramatically different ATI, for one data set, the LSTs were georeferenced in ENVI. Then, an ATI image was created and compared with the ATI image using LSTs georeferenced in ArcMap. While the georeferencing was slightly different between the two, the ATI images were relatively very similar. Furthermore, in order to determine if using albedo calculated in a different way would have an effect on the outcome, two broadband albedo images for one data set were created in ENVI with the Band Math Tool. Version 5 and version 6 of MODIS/Aqua Surface Reflectance Daily L2G 1km standard product MYD09GA was used with the algorithm from Liang (2000). Two ATI images were

created with these albedo images and were compared with the ATI image created with the MCD43B3 standard albedo product, and all three were very similar.

III.D. Fractures

Fracture mapping was performed through visual interpretation of: 1) Landsat OLI images using RGB color combinations 7-5-3, 5-4-3, and 4-3-2 with applied pan-sharpening and directional filters; 2) 40 SRTM DEM images with hill-shades at 10°, 15°, and 20° sun elevations with 360° azimuths in 15° increments and application of low-pass and Sobel filters; 3) 7 ASTER DEM images with hill-shades at 15° sun elevation between 330-030° azimuths and application of low-pass and Sobel filters; and 4) Radarsat-1 images with low-pass filters. Illumination sun angles shallower than 20° were used for the hill-shaded images to enhance structures in relatively flat regions of the study area (Peña and Abdelsalam 2006). The various data types used to create the fracture map were needed to complement each other and to avoid omission of mapping fractures if only one type of data set is used. The Landsat and SRTM images have both advantages and disadvantages for their use in lineament/fracture analysis. For instance, major north-south trending fractures cannot be distinguished in the Landsat images due to vegetation, but these are very clear in the SRTM hill-shaded DEMs. On the other hand, the fine detail available in the Landsat images is lost in the SRTM images. The Radarsat-1 data helped distinguish fractures in areas covered with thin (~2 m thick) sand due to the penetration ability of the radar data of dry sand. In addition, 10 E-W and 5 N-S topographic profiles were constructed in ArcMap to relate the topography to mapped fractures. A fracture density map was created in ArcMap by placing points along the

fracture lines in 1 km increments and then calculating the density of those points with the kernel density tool. The output is the number of points per square kilometer. One km increments were chosen to ensure that every mapped fracture would have at least one point to use in the density calculation.

III.E. Multi-map Analysis

To determine the best possible locations for future groundwater water well drilling, the fracture density, hydraulic conductivity, and thermal inertia maps were combined with an aquifer thickness map from Senosy et al. (2013). Polygons were created to map the aquifer thickness, and these polygons were then rasterized. The values for each map were reclassfied on a one to ten system, with ten being more conducive to shallow groundwater or a better producing well. Each was then added together with the weighted sum function in ArcMap to create a composite map with possible values ranging from 6 to 39; the reason for a maximum of 39 rather than 40 and a minimum of 6 rather than 4 is explained below. Each map was given equal weight in the sum. The fuzzy membership function was used as an alternative attempt to combine the four maps, where the values for each map are reclassified into a 0 to 1 scale where 1 is fully a member of a group that is likely to have shallow groundwater or good producing wells based on the variable, and 0 is not a member of that group. Values in between are "fuzzy" members of that group. Furthermore, the value of 1 is twice as likely to be a member of the group under consideration than the value of 0.5. There are various ways to weight the values before reclassification in order to best represent the data. However, the most straightforward approach of the sum function ultimately resulted in the most

32

geologically reasonable final map. The fracture density values were grouped into ten

classes based on natural data breaks because this method highlights the differences

between classes. The thermal inertia values were manually reclassified to highlight the

variability of values along the north-south fault. This fault appears to be enhancing

vertical movement of groundwater, but not uniformly along its length. The values were

chosen to parse out locations along the fault that may be better suited to groundwater

drilling than others. The aquifer thickness values are based on 60 meter contour data

provided by Senosy et al. (2013). The highest and lowest contour values were effectively

clipped to create ten classes. The hydraulic conductivity values were classified at 3, 6,

and 9 for tight, fair, and good, respectively; this yielded an overall range of values of 6 to

39 rather than 4 to 40.

CHAPTER IV

RESULTS

IV.A. Paleodrainage

The results of the paleodrainage study are shown in Figure 9. A drainage divide along the plateau edge can be seen, and the modeled drainage lines shown here are in good agreement with those that can be visually interpreted in optical remote sensing datasets along the plateau. This, coupled with the direction of flow throughout the study area, indicates this is a closed basin that could have held water in the past. One sub-basin can be seen at the very southern end of the study area. These findings are in agreement with field work of Kroplin (1993).
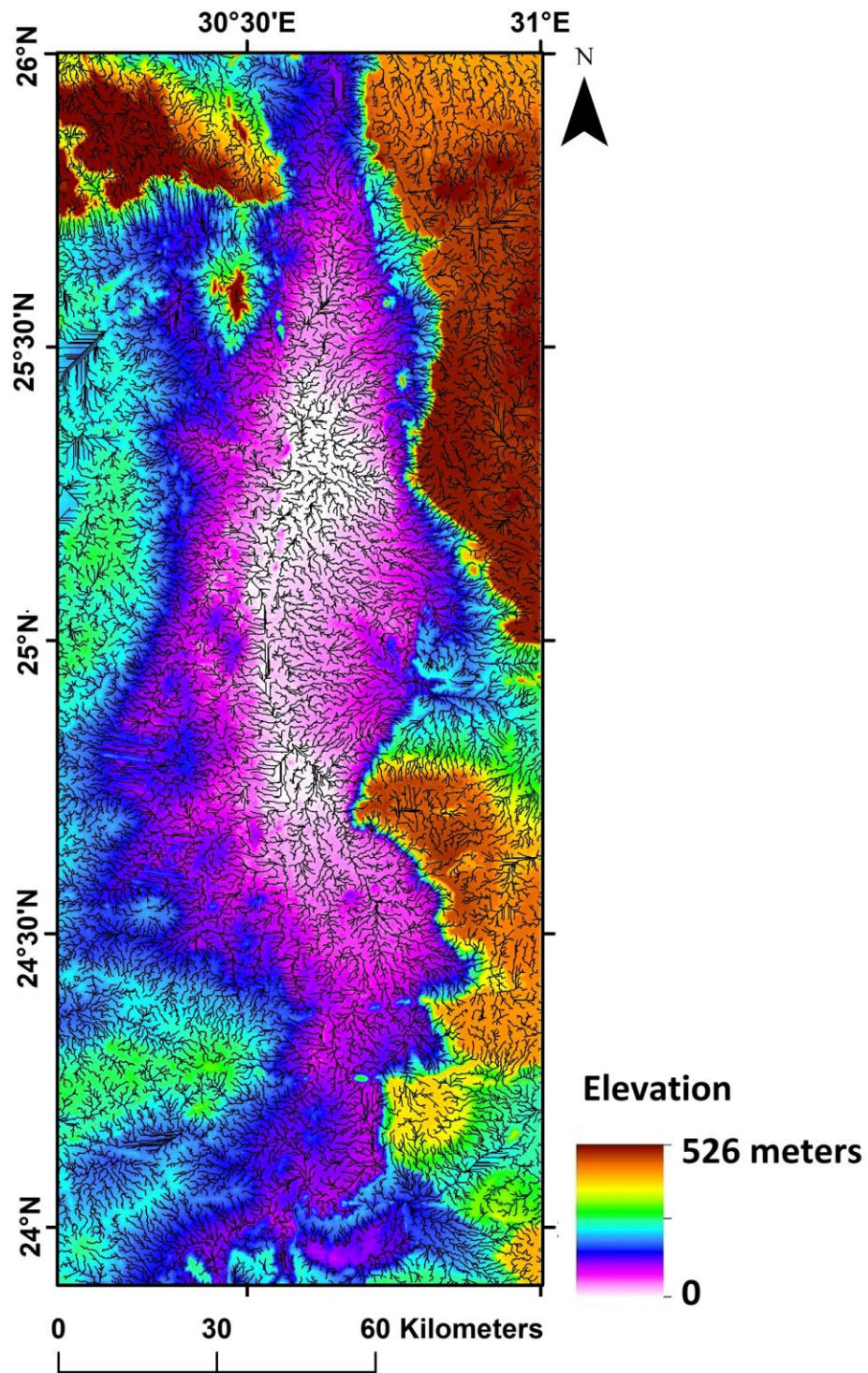
Figure 9: Paleodrainage network of the Kharga Basin. Map generated in ArcMap using
30 m spatial resolution SRTM DEM.

IV.B. Lithology and Hydraulic Conductivity

The geologic map created in this study is shown in Figure 10. The geologic boundaries mapped are consistent with previous work (e.g. Hermina 1990). Hydraulic conductivity maps of previous studies differ on the western side of the study area with the lithology presented by Hermina (1990). Figure 11 shows the hydraulic conductivity map determined from the lithology of Hermina (1990). For the western side of the study area, hydraulic conductivity values were extrapolated from the same formations in the Dakhla Basin (Hesse et al. 1987). See the discussion in Chapter V for more information
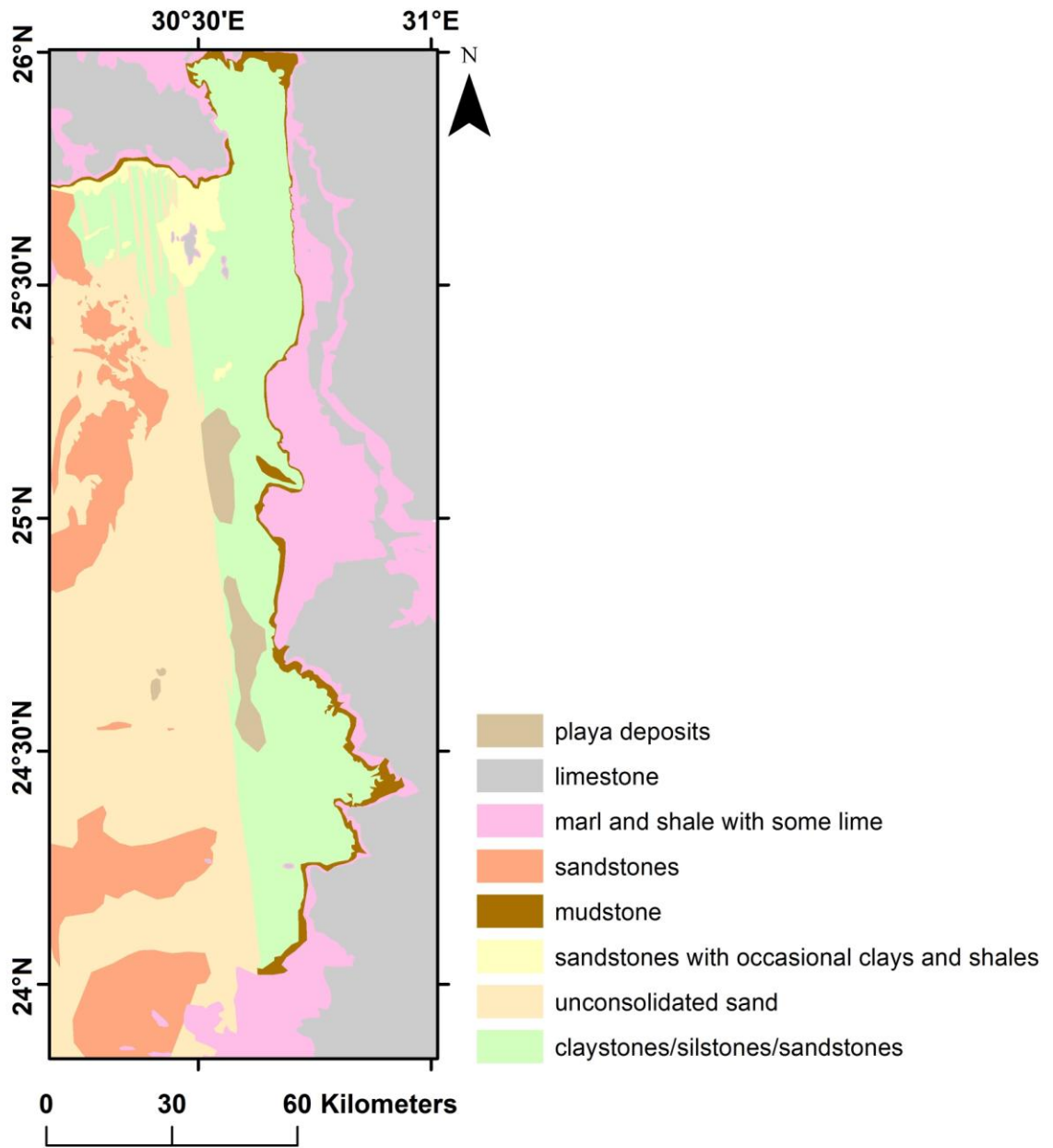
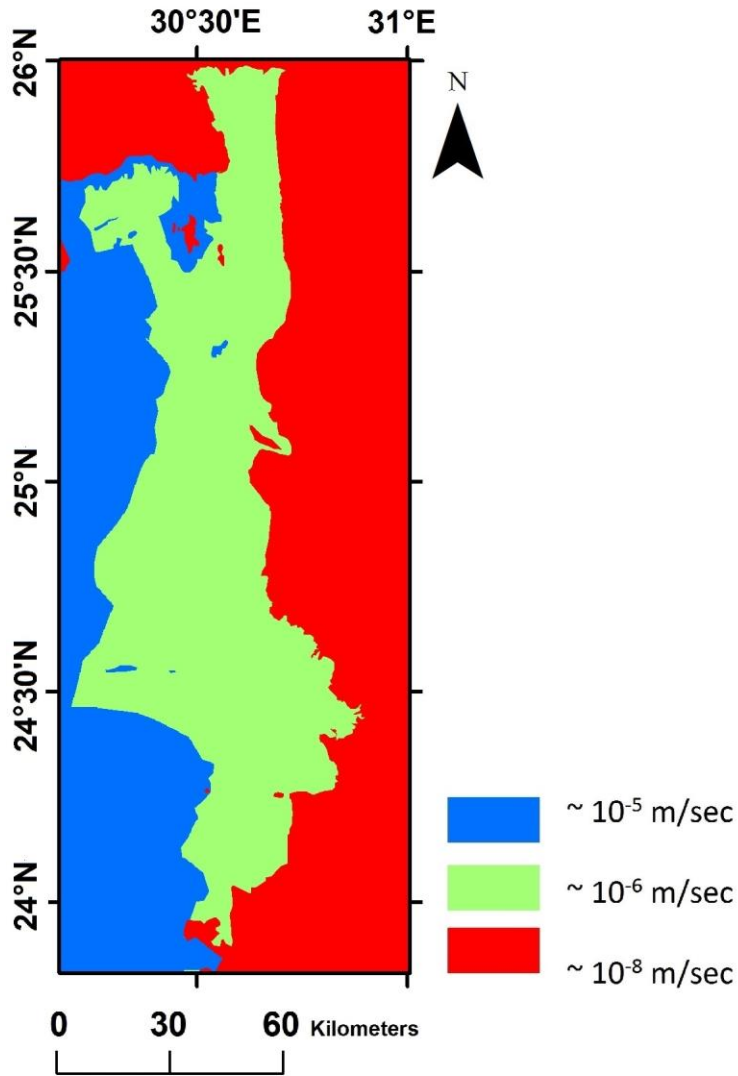Figure 10: Geologic map of the Kharga Basin. After Hermina (1990).

Figure 11: Hydraulic conductivity map of the Kharga Basin.

IV.C. Thermal Inertia

The results of the thermal inertia study are shown in Figures 12-and 13. The March 2010 data set is shown here as it had the highest ΔT and lowest and least dynamic wind speed throughout the day of all the datasets. The other three datasets have TI images similar to this one (Appendix B). Around the edges of the plateau, the modeled TI values are artificially high due to the steepness of the slope and the different times of

local maximum and minimum temperature that occur locally rather than due to higher

soil moisture. On top of the plateau itself, different lithology is the cause of the higher TI

values rather than higher soil moisture. For these reasons, the slopes and plateau have

been masked out. The black polygons represent oases or land that has been reclaimed for

agriculture through irrigation. As expected, these areas have higher TI values, and most

of these values fall within the range 800-1000 TIU that corresponds to 18-21% soil

moisture. The area to the west with higher TI values (800-900 TIU) that are not related

to the oases initially were thought to represent locations where fractures may have

facilitated the vertical movement of groundwater. However, upon further investigation,

Landsat OLI images showed that these areas are dominated by bedrock outcrops rather

than unconsolidated sediment. Once again, the lithological difference is the cause of the

higher thermal inertia values, not an increase in soil moisture. There may be a slight

slope effect increasing the values as well. There are slightly higher TI values along the

east-west fault near ~24°30' suggesting this fault may facilitate the vertical movement of

groundwater. Aside from this fault and the main north-south fault, the thermal inertia

study did not result in any fractures that seem to serve as vertical conduits bringing

groundwater to the very shallow subsurface. Figure 13 shows a density slicing of thermal

inertia values. Almost all areas of vegetation have a thermal inertia value over 800 TIU.

This map shows the southern end of the fault is more conducive to the expansion of

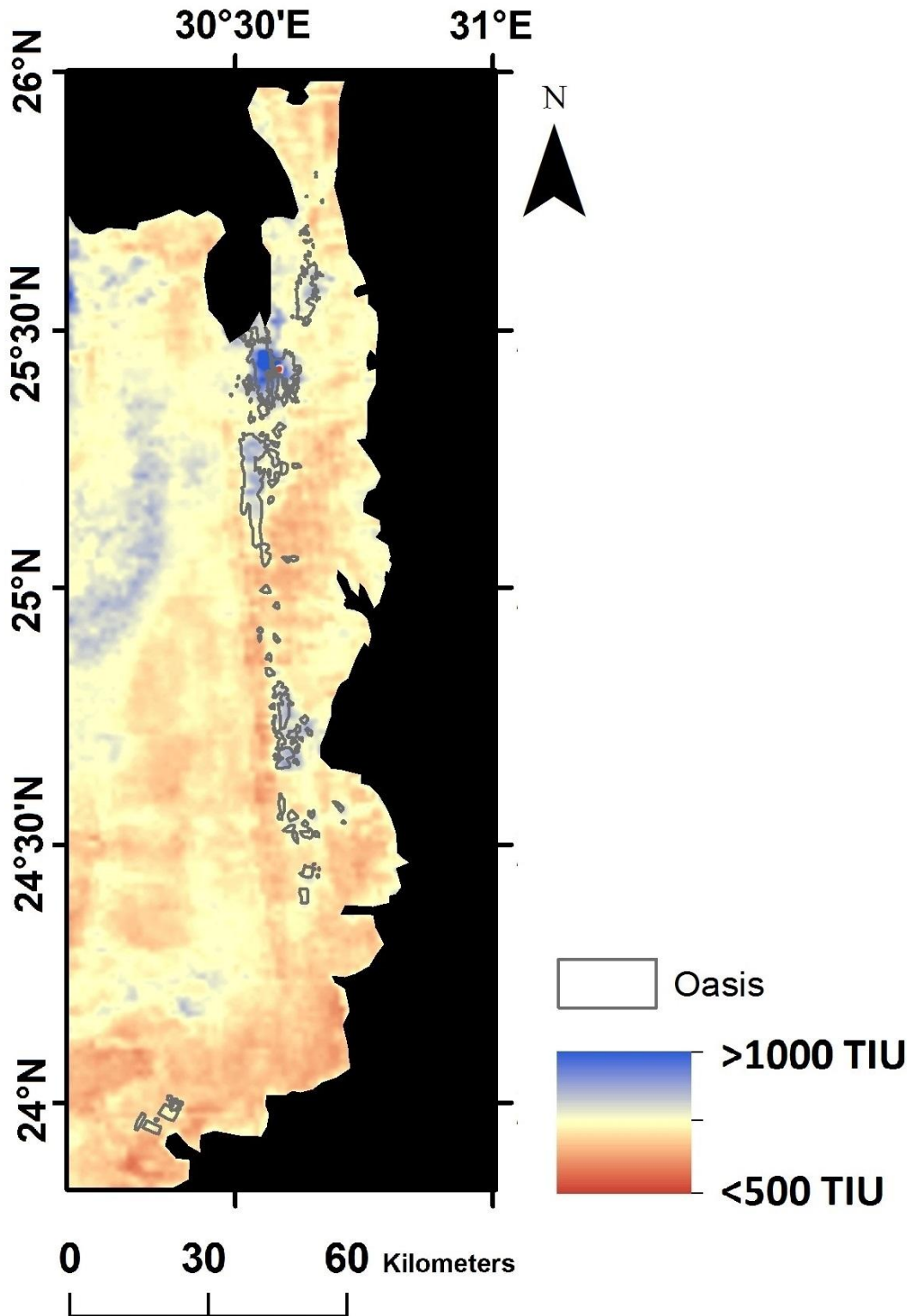groundwater drilling projects than in the center of the fault.

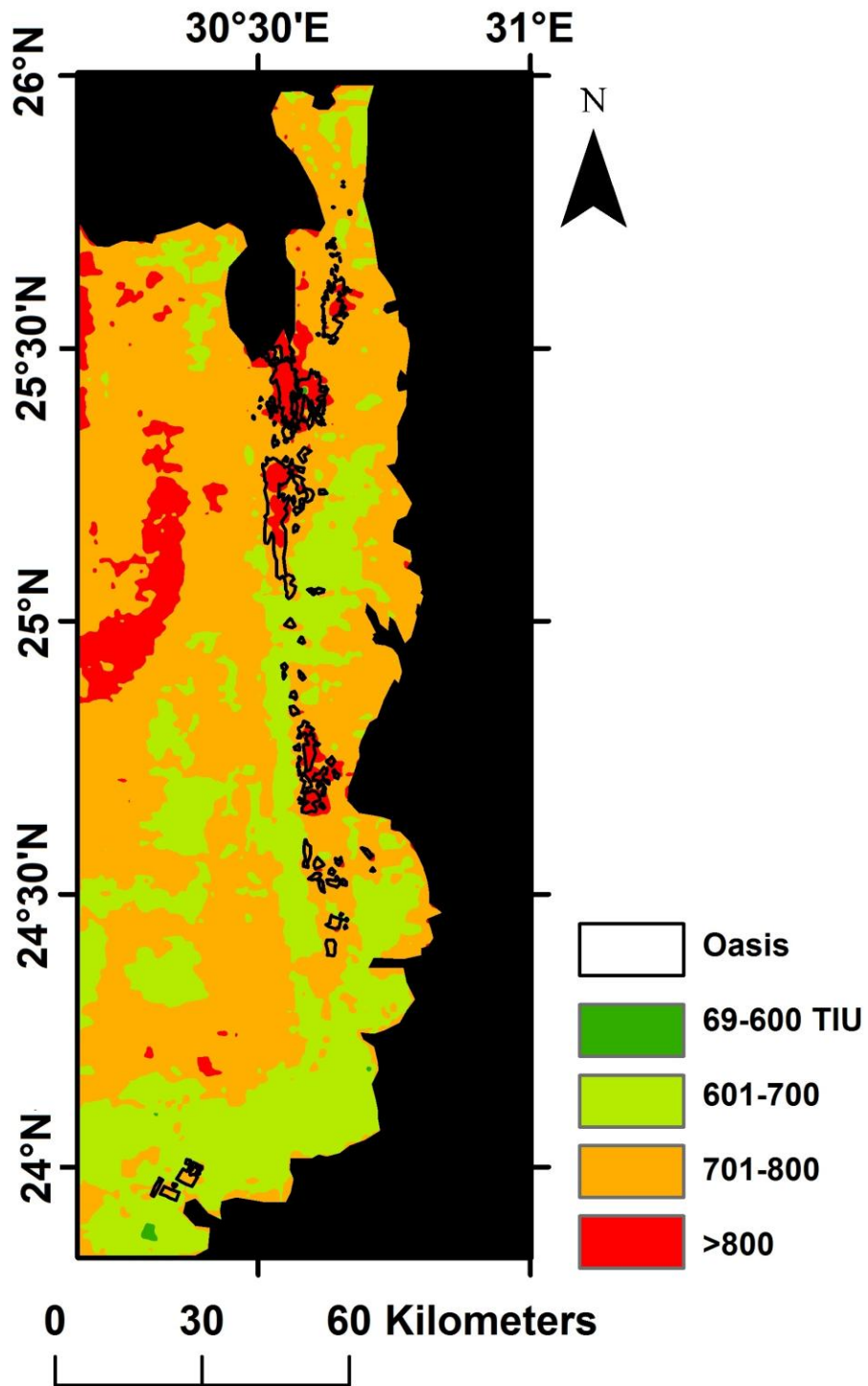Figure 12: Kharga Basin thermal inertia derived from March 2010 data.

Figure 13: Density-sliced Kharga Basin thermal inertia derived from March 2010 data.

IV.D. Fractures

The fracture map was overlain on a SRTM DEM and is shown in Figure 14. A rose diagram of these fracture trends is shown in Figure 15. The predominant trends are N-S and E-W, which is in good agreement with fracture trends mapped by Hesse et al. (1987). The fracture density map (Figure 16) shows some areas of promise for groundwater drilling in the southern portion of the basin given that high fracture density can be related to a shallow groundwater water table (Anudu et al. 2011).

Figure 17 shows the location of the topographic profiles illustrated in Figures 18 - 20. Based on topography, most of the fractures have been interpreted as fault scarps. The steep dip angle of the drawn faults is due to vertical exaggeration (50X). Due to the tectonic history of the area, normal faults in this area are expected to dip ~60°.
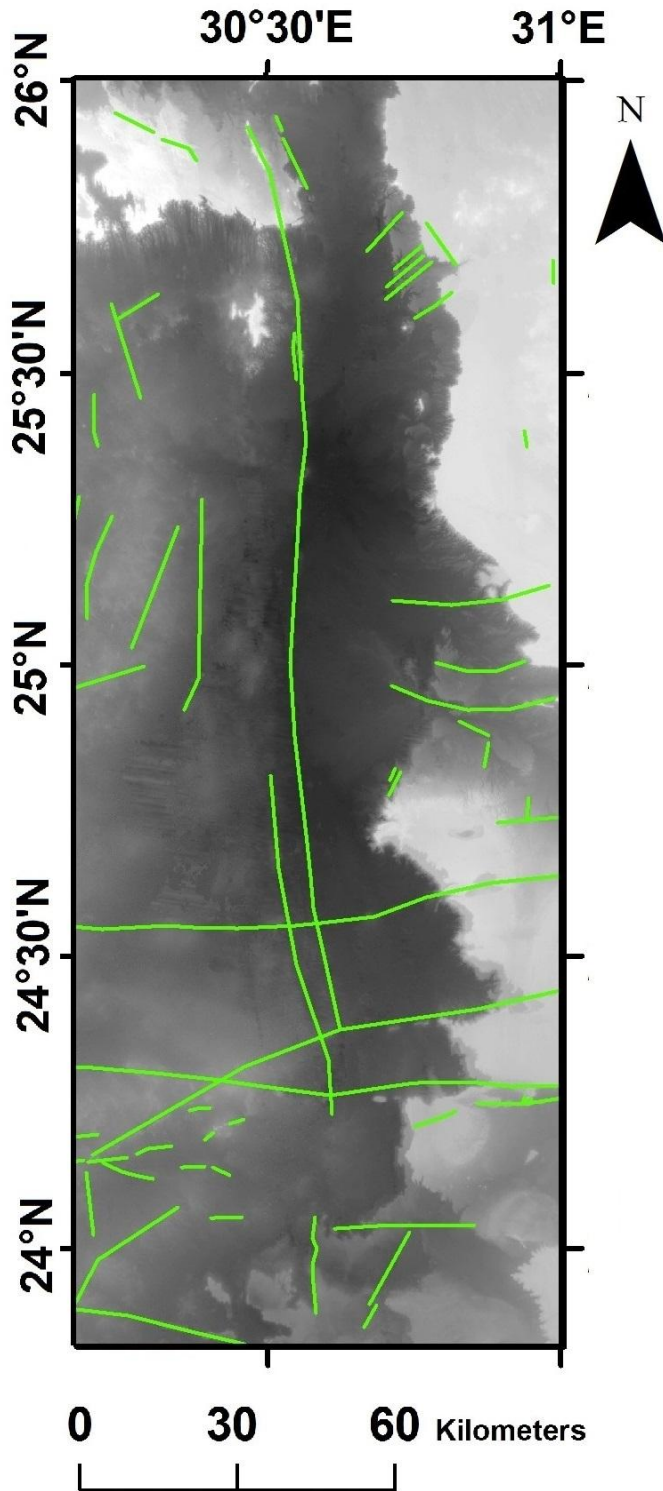
Figure 14: Fracture map of the Kharga Basin. Fractures inferred from SRTM, ASTER, Radarsat-1, and Landsat OLI datasets; basemap is SRTM DEM.
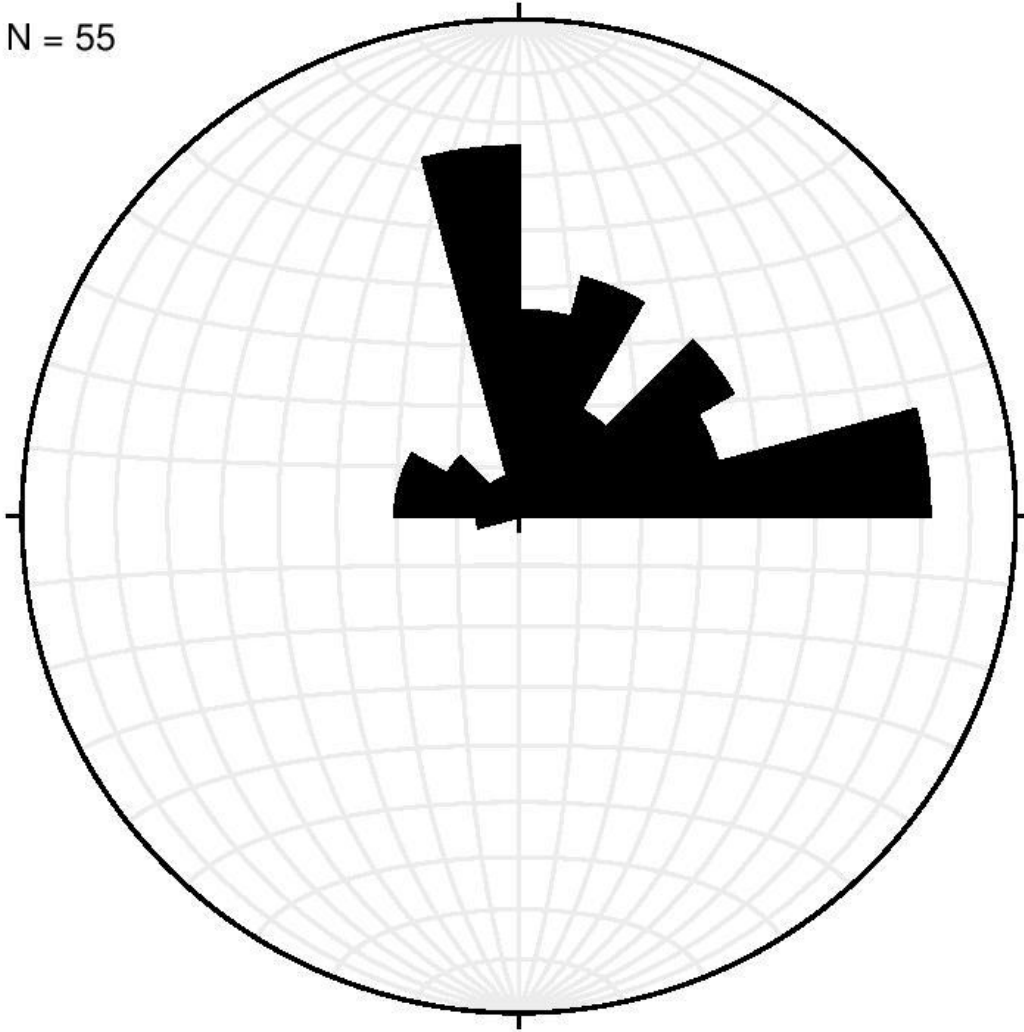
Figure 15: Rose diagram of fracture trends of the Kharga Basin. Data from Figure 14.
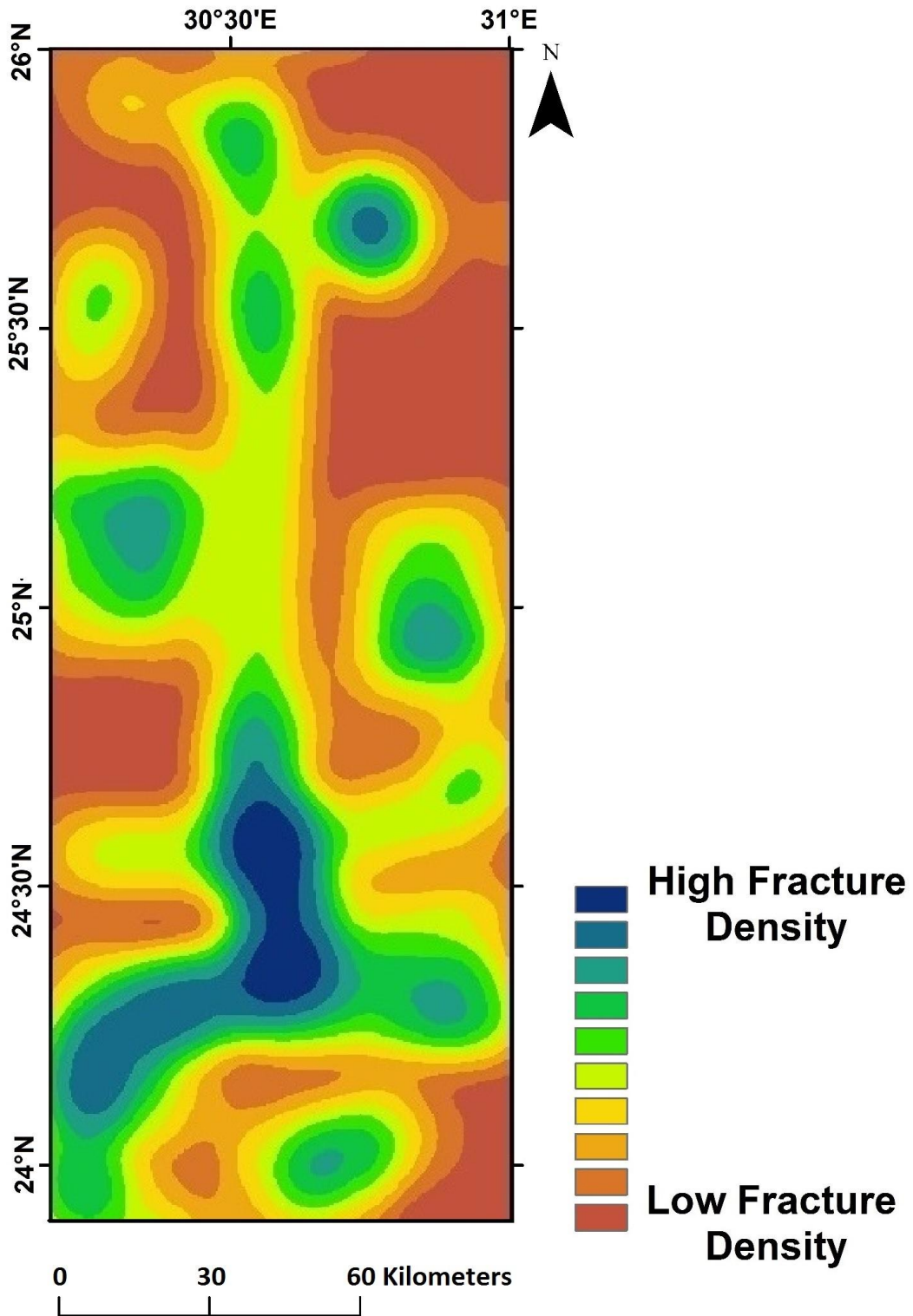
Figure 16: Fracture density map of the Kharga Basin. Contours are drawn based on natural breaks in the data.
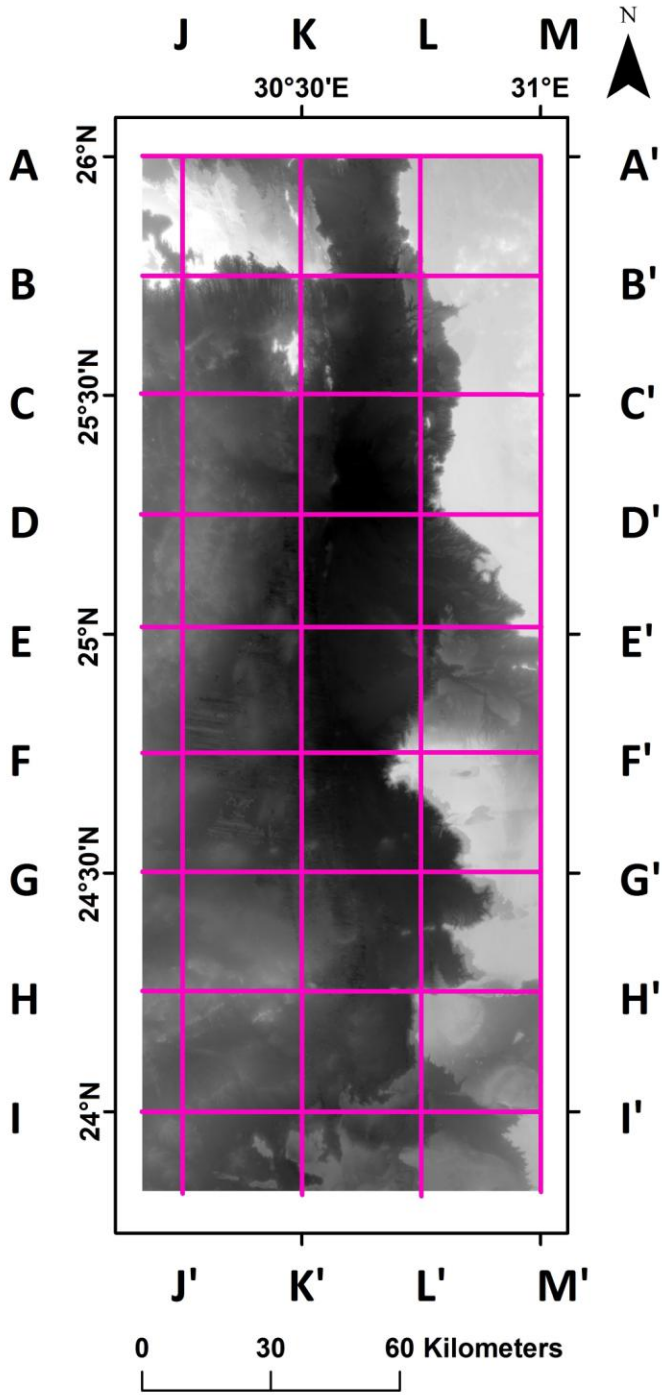
Figure 17: Topographic profile locations. Basemap is 30 m spatial resolution SRTM

DEM.
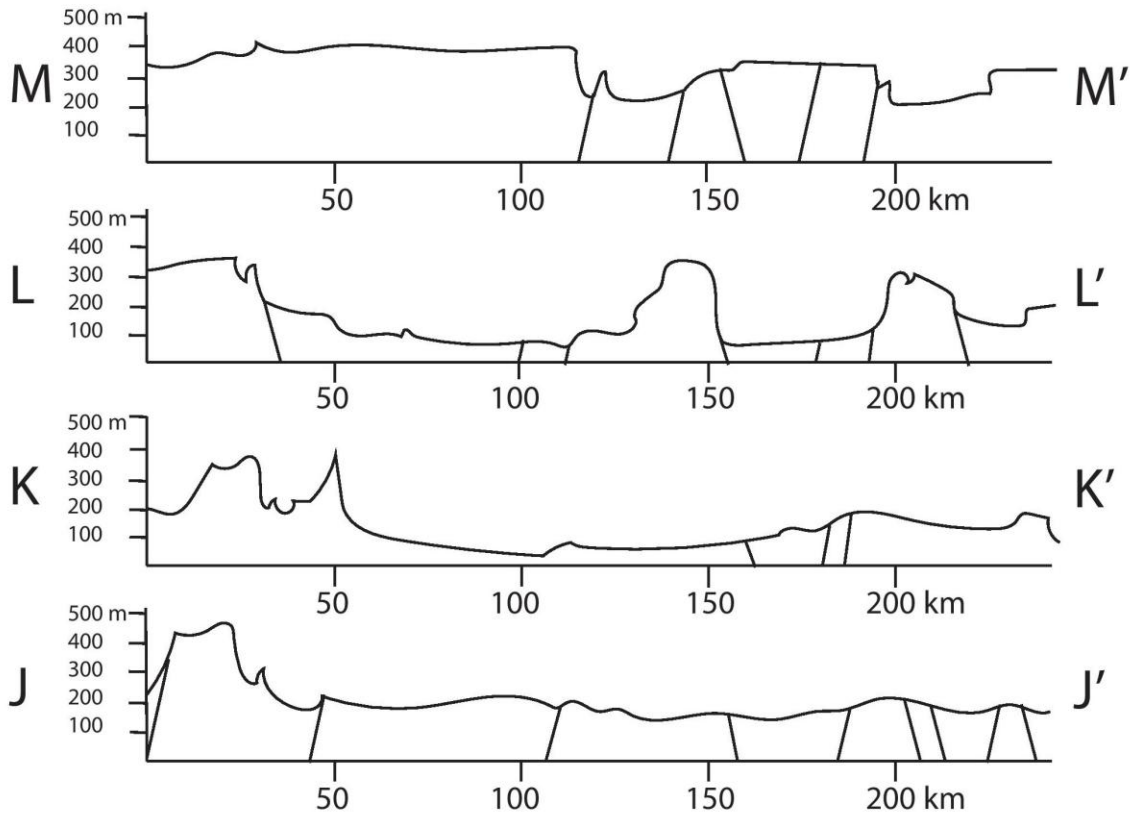
Figure 18: N-S topographic profiles with inferred fractures. 50X vertical exaggeration.
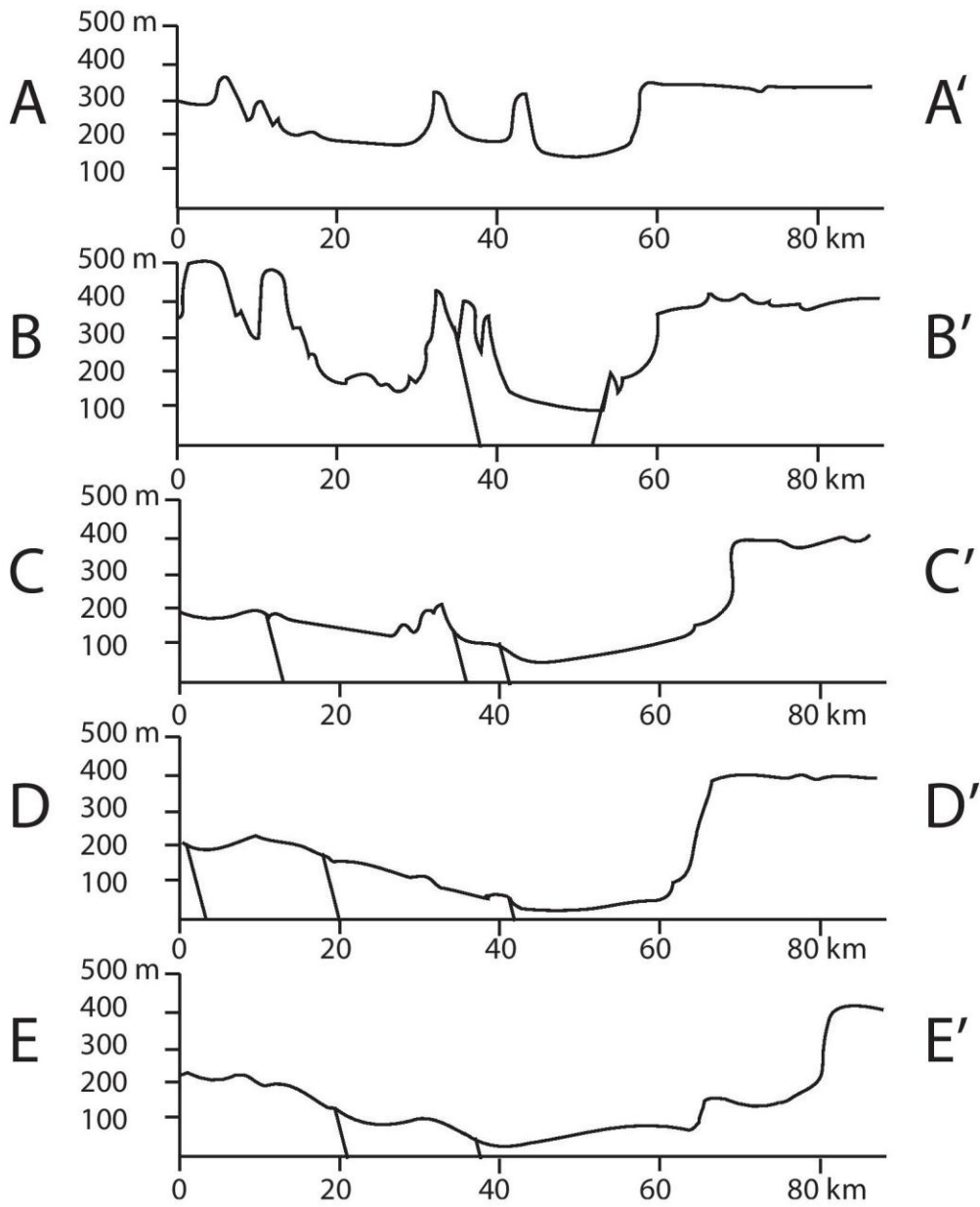
Figure 19: Northernmost W-E topographic profiles with inferred fractures. 50X vertical exaggeration.
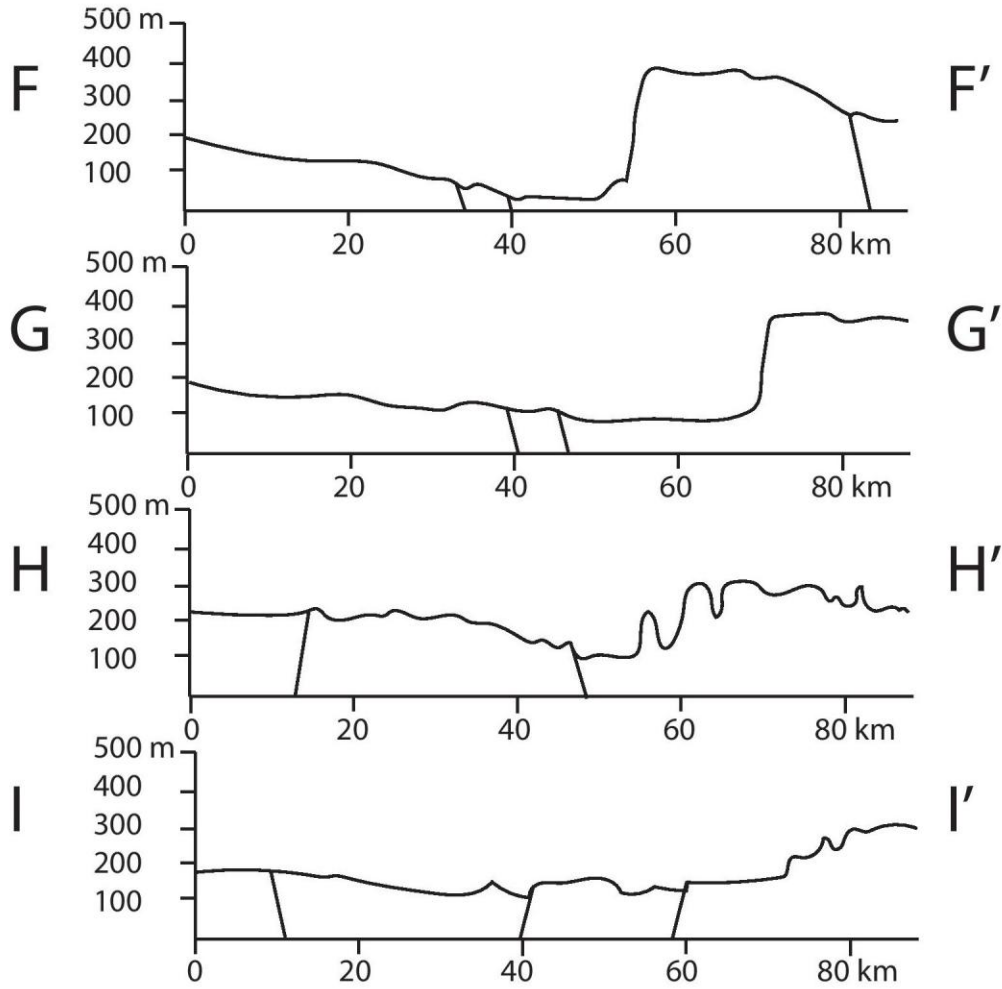
Figure 20: Southernmost W-E topographic profiles with inferred fractures. 50X vertical exaggeration.

IV.E. Multi-map Analysis

The aquifer thickness map created after Senosy et al. (2013) is shown in Figure 21. This map combined with the fracture density, hydraulic conductivity, and thermal inertia maps shown previously resulted in the final map shown in Figure 22. The entire study area is not conducive to economic groundwater drilling when considering land and

economic factors. Figure 23 has the areas of poor land suitability masked out (after

Alaily and Blume 1993). Sand dunes and the plateau make up most of these areas.

Figures 24-26 have masked out areas that were uneconomic based on 2005, 2020, and

2060 hydraulic head contours, respectively (after Mahmod et al. 2013). The hydraulic

head contours were overlain on an SRTM DEM to determine the areas that would be

uneconomic based on the pumping depth of 38 meters (Ebraheem et al. 2003). Based on

the groundwater model of Mahmod et al. (2013), cones of depression will greatly affect

the study area, particularly to the north. Although the economic pumping depth may

increase in the future, it is important to consider future drawdown in the placement of

wells. The results of this study show areas in blue or green that are better suited to

groundwater well drilling based on the four input variables (Figures 22-26). Projected

drawdown further constrains these areas, but there are locations that could support more

groundwater wells.
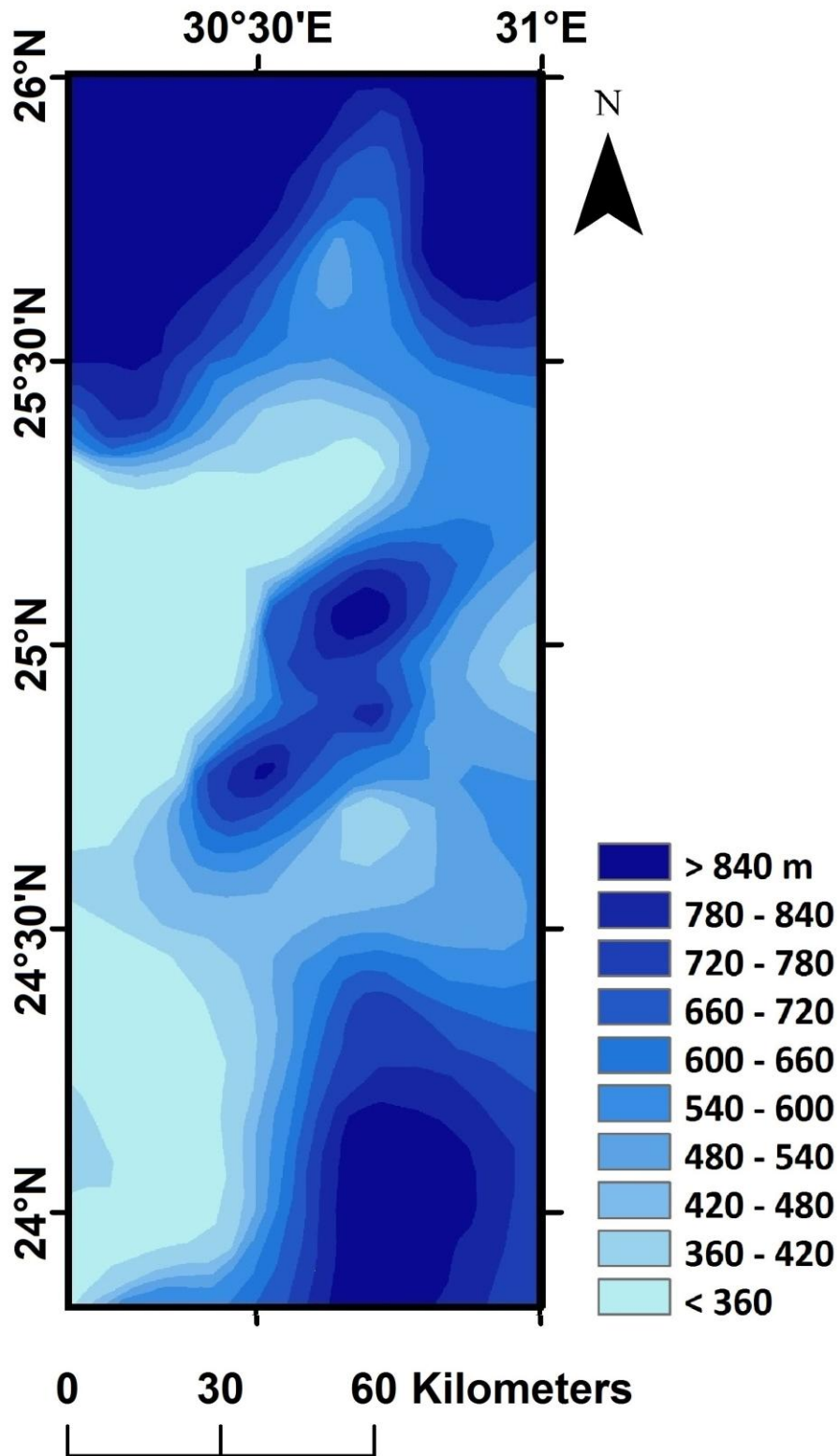
Figure 21: Aquifer thickness of the Kharga Basin. After Senosy et al. (2013).
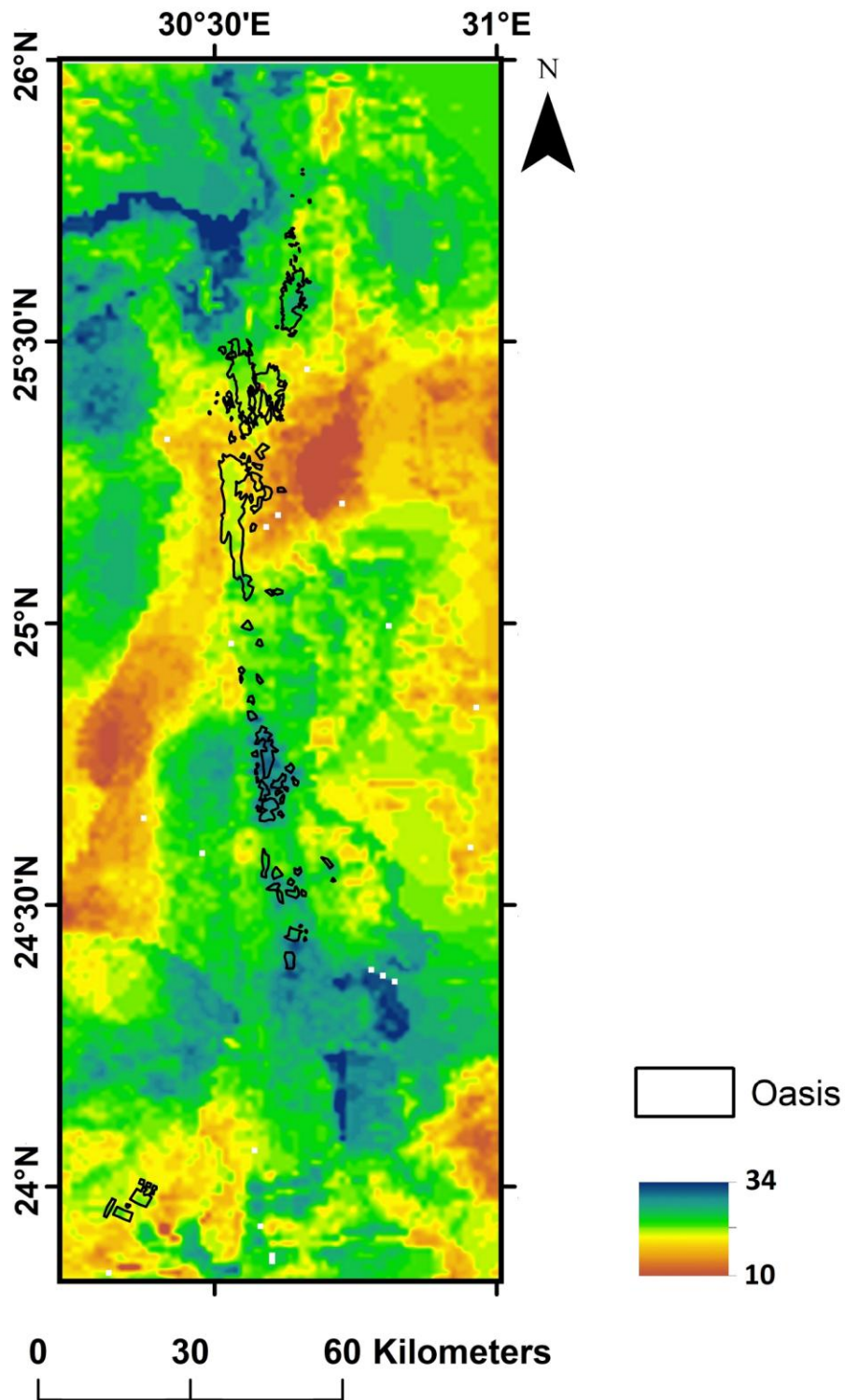
Figure 22: Multi-map analysis for groundwater potential of the Kharga Basin. High value locations are more likely to allow productive water wells.
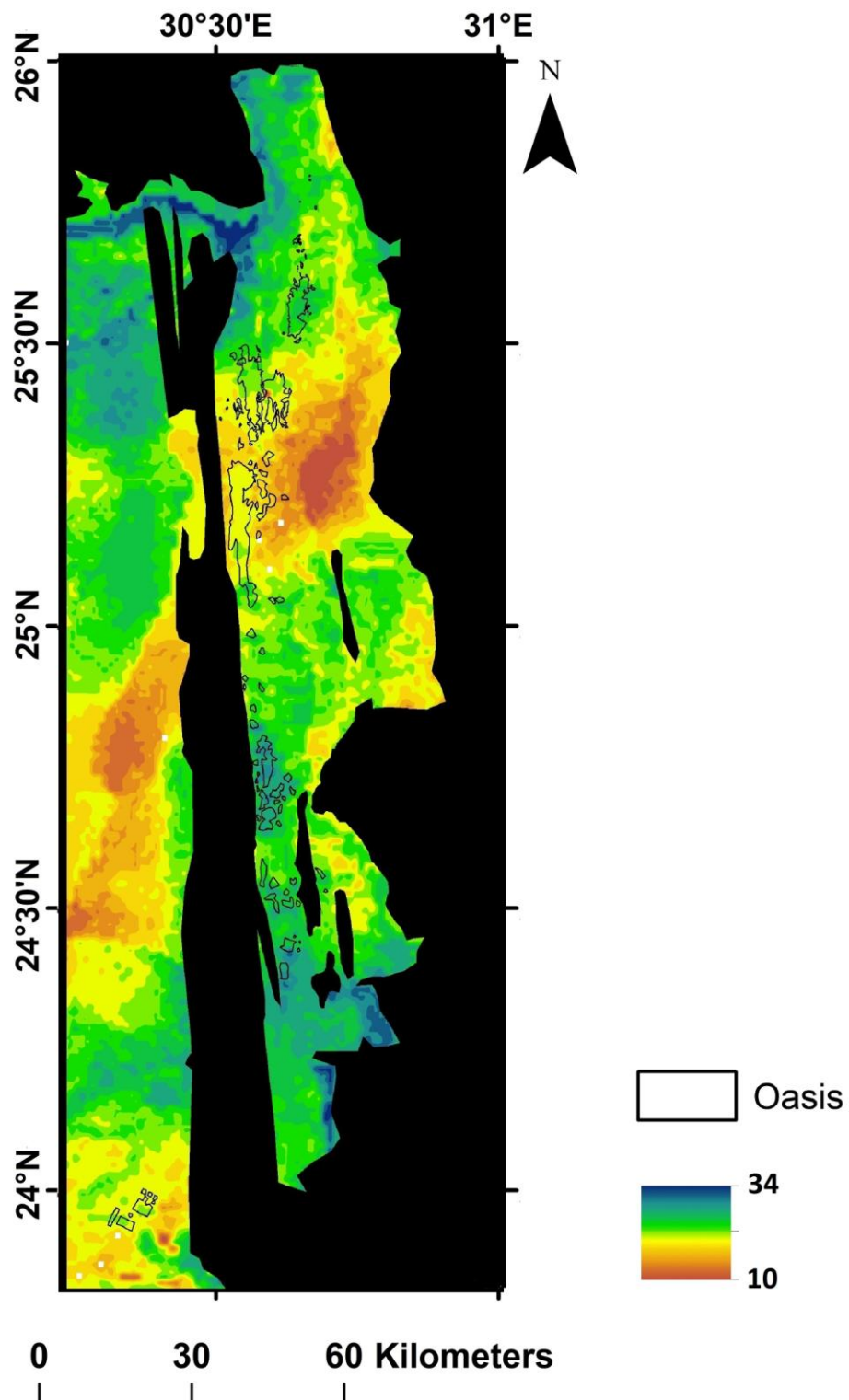
Figure 23: Multi-map analysis for groundwater potential of the Kharga Basin with poor land suitability masked out. Land suitability after Alaily and Blume (1993).

Figure 24: Multi-map analysis for groundwater potential of the Kharga Basin with poor land suitability and uneconomic areas in 2005 masked out. Land suitability after Alaily and Blume (1993); 2005 economic areas after Mahmod et al. (2013).

Figure 25: Multi-map analysis for groundwater potential of the Kharga Basin with poor land suitability and uneconomic areas in 2020 masked out. Land suitability after Alaily and Blume (1993); projected 2020 economic areas after Mahmod et al. (2013).
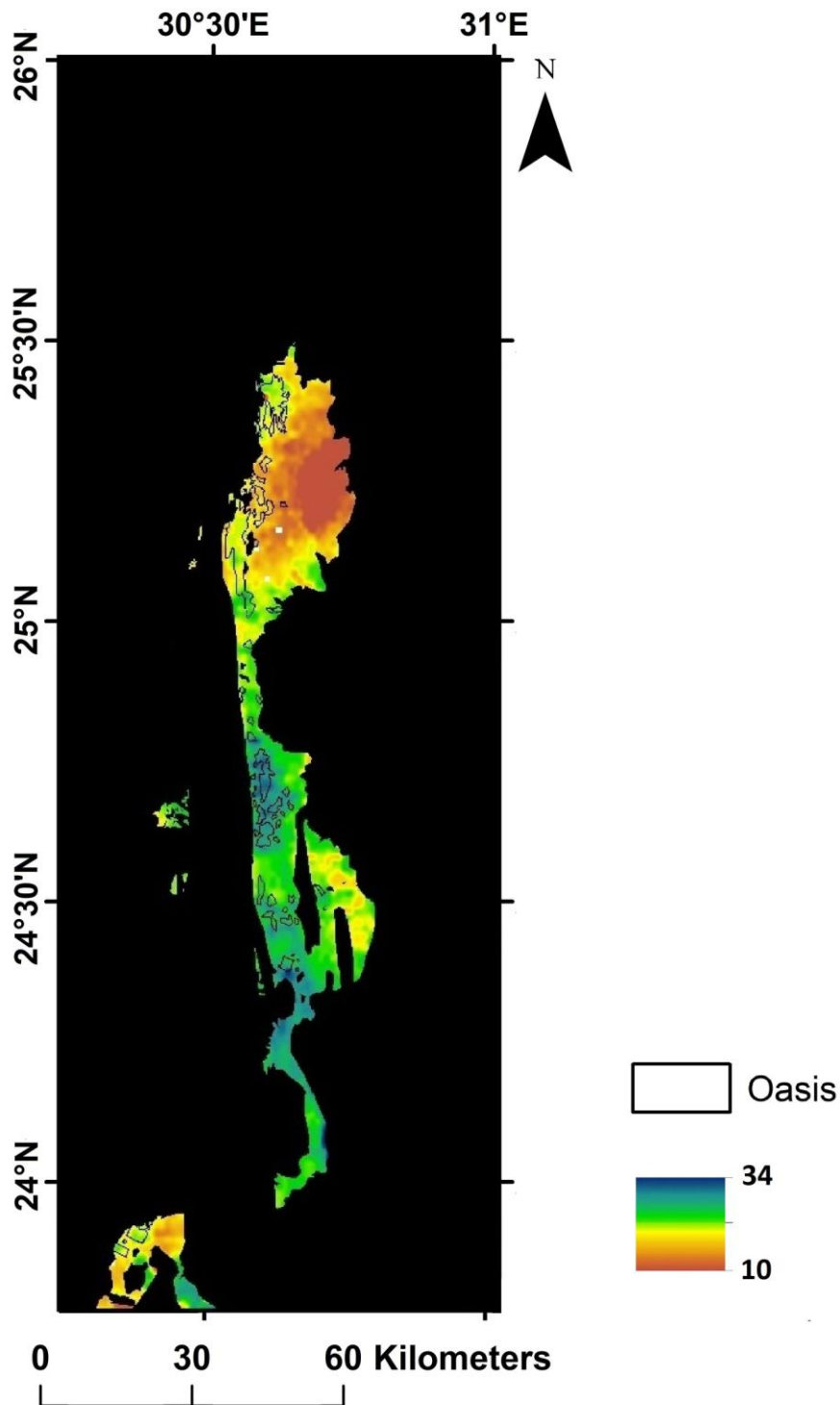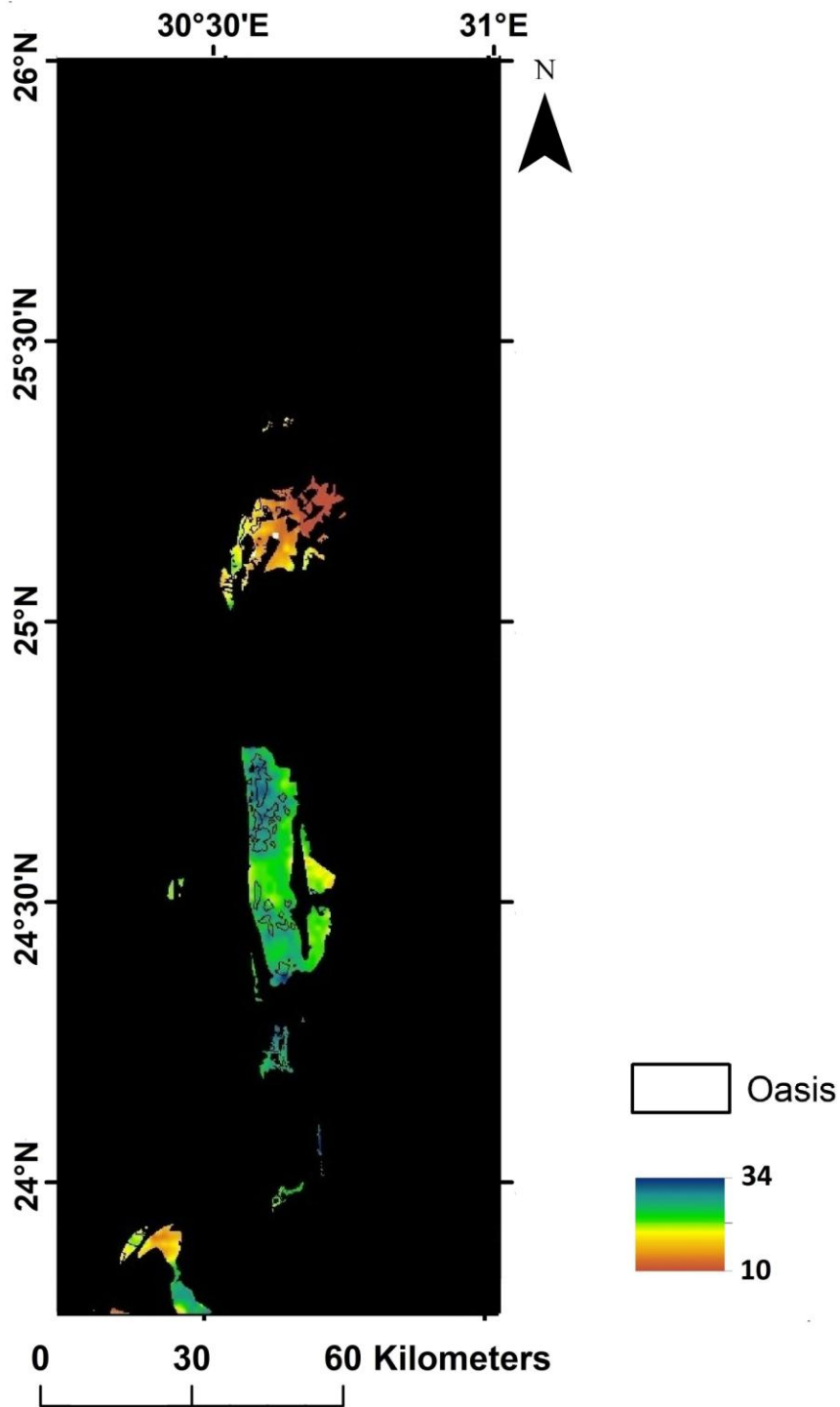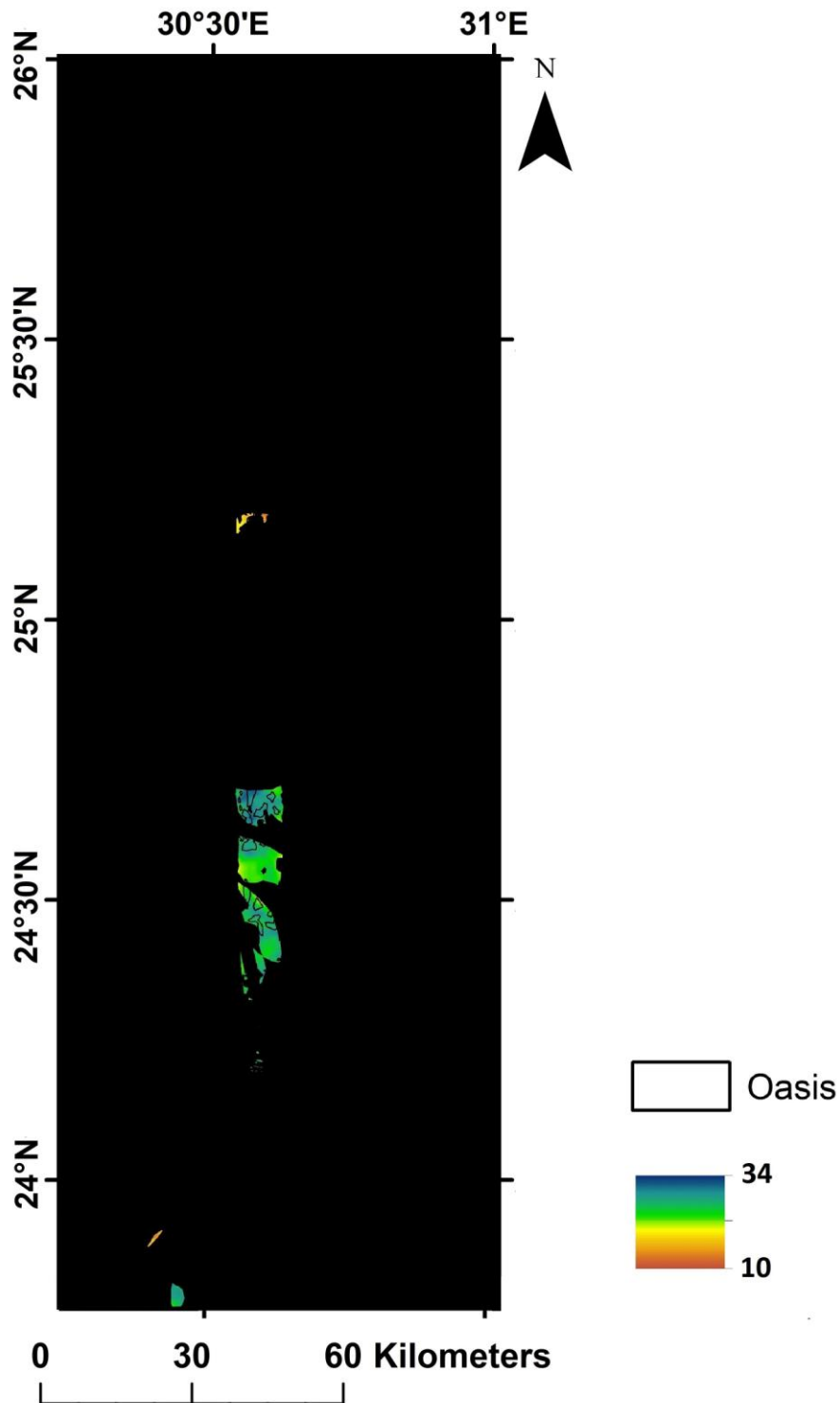
Figure 26: Multi-map analysis for groundwater potential of the Kharga Basin with poor land suitability and uneconomic areas in 2060 masked out. Land suitability after Alaily and Blume (1993); projected 2060 economic areas after Mahmod et al. (2013).

CHAPTER V

DISCUSSION AND CONCLUSIONS

V.A. Discussion

Mapping the drainage network of the Kharga Basin is difficult because of the sand cover. The drainage network in the deeper portion of the Kharga Basin is buried beneath dunes and sand cover. No radar system has fully penetrated this thick unconsolidated sand accumulation although past studies have been able to image some channels with the SIR system (e.g. McCauley et al. 1982). The SRTM DEM used in this study is a surface model that does not penetrate the sand. Furthermore, many of the paleochannels (mapped in Figure 9) that were flowing towards the Kharga would have terminated at the shores of the Kharga "paleo-lake" before reaching the basin floor if there was a standing body of water that filled the basin. Evidence for lakes at 247 m and 190 m elevation can be seen through such channel terminations (Maxwell et al. 2010). However, along the plateau edge sand cover is not an issue. The goal of the drainage mapping of this study was not to obtain a detailed network of drainage lines within the basin, but to establish that Kharga is a closed basin that could have held water in the past as suggested by previous studies (e.g. Robinson 2002; Maxwell et al. 2010). The drainage network and divide seen along the plateau is consistent with those developed

during the late Pleistocene and earlier Holocene humid periods.

Further evidence for the presence of two large lakes and other smaller lakes during past pluvial episodes include fossils, lake carbonates, playa deposits, tufas, and archeological artifacts (McHugh et al. 1988; Pachur and Hoelzmann 2000; Smith et al. 2004a,b; Kieniewicz and Smith 2007; Smith et al. 2007; Maxwell et al. 2010). Maxwell et al. (2010) suggests overflow of the Nile coupled with local rainfall had led to the formation of these paleo-lakes. Evidence of overflow of the Nile leading to lakes within depressions in the Western Desert has been seen recently. In 1998, an overflow from Lake Nasser resulted in the formation of the Tushka lakes (the New Lakes of Sahara) just south of the study area (Abdelsalam et al. 2008; Bastawesy et al. 2008). The fact that lakes can form in the desert during the present hyper-arid phase indicates that formation of larger lakes during more humid periods is possible. The existence of multiple lakes in the study area throughout the past 300,000 years that held significant amounts of standing water for a long period of time is also indicative of the presence of a saturated aquifer that has been completely recharged multiple times. Heinl and Brinkmann (1989) stated that the depressions throughout Egypt's Western Desert have always been areas of outflow, not areas of recharge because of the high groundwater table within the saturated aquifers.

Because of the south-to-north hydraulic gradient, it is estimated that at the average velocity of 1 m/yr of groundwater movement through sandstones (Gossel et al. 2004), it would take 220,000 years for all water from the southern end of the Kharga Basin to completely move to the northern end of the basin. At this rate, water that recharged the aquifer from the last four pluvial episodes would still reside within much of

the Nubian Sandstone Aquifer underlying the basin, including that of the two large lakes described by Maxwell et al. (2010). This indicates there is still a significant amount of groundwater to be used in the region.

The geologic map created in this study is combined with published hydraulic conductivities of formations from the Dakhla Oasis and hydraulic conductivity maps (e.g. Hesse et al. 1987; Thorweihe 1990; Ebraheem et al. 2002), to produce a hydraulic conductivity map for the Kharga Basin (Figure 10). Hesse et al. (1987) show only fair and tight hydraulic conductivity at the surface in the Kharga area. However, a lithologic map from Hermina (1990) shows formations outcropping west of the Kharga Basin that correspond to formations detailed by Hesse et al. (1987) in the Dakhla Basin. According to Hesse et al. (1987), the Dakhla Basin equivalent of the sandstone formations that crop out west of the Kharga Basin have hydraulic conductivities of 10^{-5} m/sec, which would classify them as having good hydraulic conductivity It is fair to assume that the hydraulic conductivity measured in the Dakhla Basin could be applied to the same formation in the Kharga Basin. This notion corresponds with the transmissivity map of Thorweihe and Heinl (1993) showing increasing transmissivity towards the west. Hermina (1990) has mapped the Sabaya, Six Hills, and Taref Formations to be cropping out west of the Kharga Basin. Although Hesse et al. (1987) does not have a formation map for this area, the hydraulic conductivity is listed as lower than would be expected for these formations. The Sabaya and Six Hills Formations cropping out just to the west of the Kharga Basin are clean sandstones without the clay seen in the basin area, and the Taref Formation has only minor clays/shale content. A higher hydraulic conductivity in these areas could lead to a higher transmissivity if the saturated thickness is high. Figure

20 shows that some areas in the western part of the Kharga Basin have thicker sedimentary sections. Currently, the elevation, hydraulic head, and economic pumping depth make these locations uneconomic. However, it is important to consider the higher hydraulic conductivity of these areas if the economic pumping depth increases in the future. The boundary between the good and fair hydraulic conductivity is difficult to constrain because it is obscured by the overlying sand. Nonetheless, the proposed location of this boundary is considered reasonable because of its manifestation by topographic expression in the DEM.

Apparent thermal inertia determined through remote sensing is sensitive to permeability in the top 10 cm of the ground (Pratt and Ellyett 1979). Therefore, the thermal inertia results suggest the capillary fringe of the groundwater table, whether facilitated through the vertical movement of fractures or not, is present in the near surface only along the major north-south fault and possibly the east-west fault at ~24°30'. There are some locations close to current producing wells and areas covered with vegetation that have a similar thermal inertia. It is possible that future wells drilled in those areas would have similar groundwater productivity as the existing wells, particularly in the southern end of the main oasis areas. Alternatively, not all areas of producing wells and vegetation have exceptionally high thermal inertia values, particularly the reclaimed area to the far southwest. This suggests productive farms can be located in places that are not necessarily ideal in terms of thermal inertia. It is possible that irrigation is the cause of the higher thermal inertia values in the farmed areas rather than the depth level of the groundwater table. However, it is clear that there is a distinct thermal inertia peak along the entire length of the north-south trending fault in the central part of the Kharga Basin

even in areas of no farming activity. This suggests that this fault is enhancing

permeability along its length.

The lack of higher thermal inertia values in the Kharga Basin (except along the

north-south trending fault and one east-west trending fault) does not necessarily indicate

the absence of vertical movement of groundwater along other fractures. The elevation of

the topographic surface expression of the other fractures is a factor to be considered in

explaining the lack of their association with higher thermal inertia values even in the

presence of upward vertical movement of groundwater. The surface expression of the

major north-south trending fault is found at a lower elevation than all the other fractures.

Because the thermal inertia can only capture soil moisture differences very near the

surface, upward vertical movement groundwater could be taking place at depths that are

not shallow enough to be detected by the thermal inertia modeling. It is apparent that

there is a line of vegetation that follows the main north-south trending fault rather than

following the zones of the lowest elevation along the north-south axis of the Kharga

Basin. This presents further evidence in support of enhanced groundwater transmissive

properties of this fault. The areas near this fault are still at a low elevation, but the area to

the east of the main oasis around the city of Kharga is some 20 m lower in elevation and

hosts no vegetation. There is a region in the middle of the north-south trending fault

where only very little vegetation is found. This region has a slightly higher elevation

than the portion of the fault directly to the north and south of it, but it is not the area of

highest elevation along the fault. Much of the far northern vegetated area is higher in

elevation than this region in the middle of the fault. Because of this, it seems that the

fault is not equally transmissive along its entire length. Perhaps a discontinuous shale in

the central portion of the study area combined with fault movement led to a shale smear that reduced its transmissive property. Thermal inertia values (Figures 12-13) suggest that the southern end of the fault should have a shallower water table than its central part. This is because the higher thermal inertia values characterizing the southern part of the fault suggest the presence of higher soil moisture possibly due to upward seepage of groundwater to a shallow level. Furthermore, based on the current distribution of the producing wells in the area, there is potential for future expansion of drilling projects in the south (Figure 27).

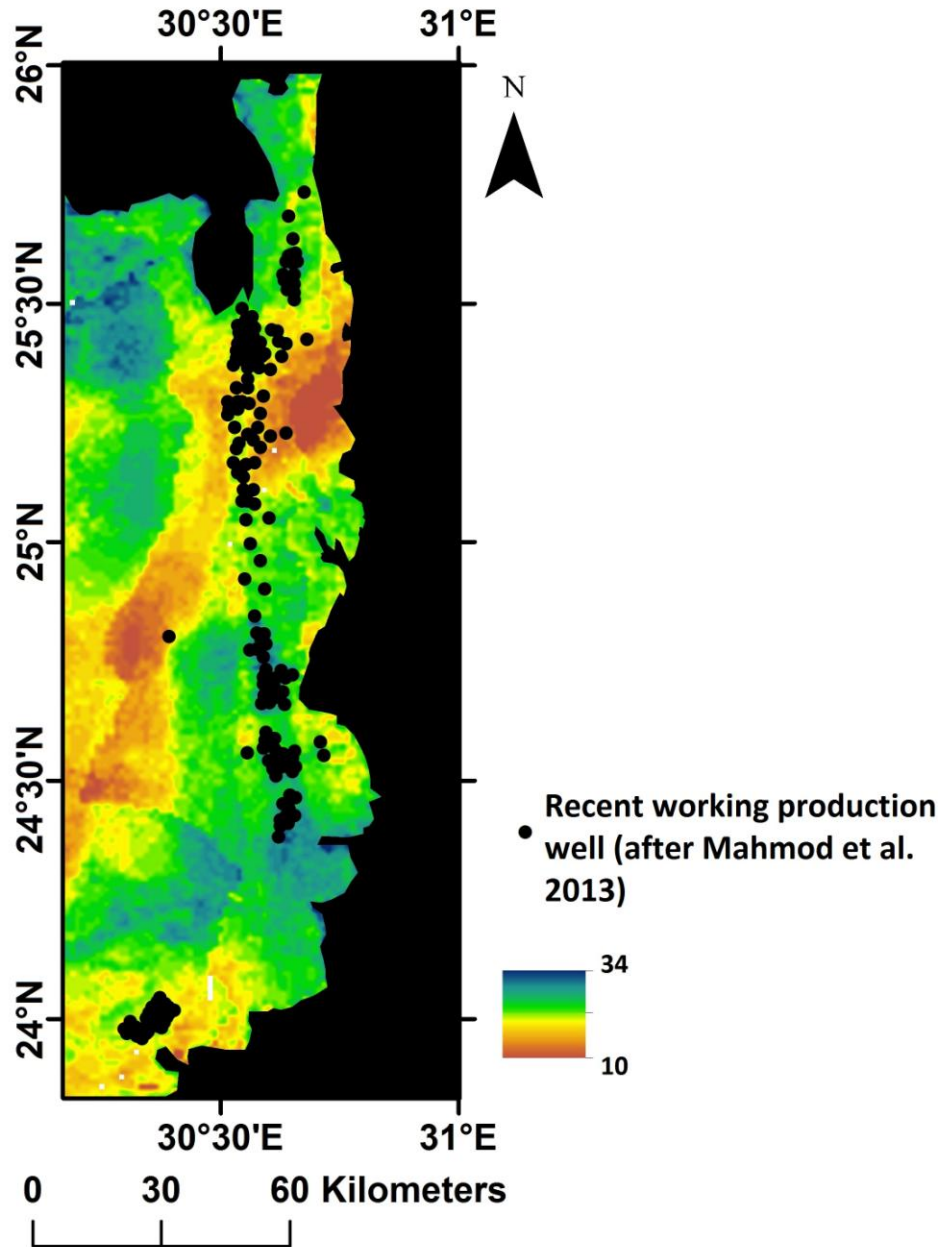Figure 27: Recent productive water wells. Basemap is result of multi-map analysis.

Despite a lack of strong spatial correlation between elevated thermal inertia

values and fractures within the Kharga Basin (other than the main north-south trending

fault and one east-west fault), fracture density should still be considered as a factor in

future geospatial analysis aimed at predicting drilling sites of successful wells of

groundwater extraction. To the south of the Kharga Basin, around latitude 23°N, east-west trending fractures are marked by vegetation and evaporite deposits indicative of upward vertical movement of groundwater (Hesse et al. 1987). It is likely these east-west trending fractures are of the same tectonic origin as those in the Kharga area indicating the plausibility of upward vertical movement of groundwater along them.

The multiple-map analysis (Figures 22-26) delineated portions of the Kharga Basin that are predicted to be very conducive to supporting producing wells. However, there are some areas in Figure 22 that are considered desirable for drilling for inaccurate reasons. For the reasons discussed previously about the thermal inertia maps, areas of high TI values not associated with relatively high soil moisture (due to slope-induced artifacts or lithology) yield higher values in the final multi-map analysis. Fortunately, these areas are excluded once the areas of land unsuitability and the uneconomic areas based on 2005 hydraulic head contours are masked. Therefore, Figure 24 better delineates areas that should be considered for water drilling projects.

Sand dune movement in the area is of major concern when it comes to establishing new settlements in the Kharga Basin. These dune belts move at a rate of 20-100 m/year (Embabi 1982). Any future planning of settlements needs to take into consideration the rate of movement of sand dune belts in that particular area (Embabi 1982). Only areas of absolute land unsuitability are masked in Figure 23. There are sites within the remaining area that are identified as suitable that still have challenges to overcome.

The maps in Figures 24-26 are all based on the value of 38 meters to be the maximum economic pumping depth (Ebraheem et al. 2003), but this depth might change

in the future and may not have been applicable to all areas in the past. The 2005 groundwater hydraulic head contours mapped by Mahmod et al. (2013) were calibrated using up-to-date data from that time period. Based on their contours and the published economic pumping depth at that time, certain areas of the northern oases would have been "uneconomic" in 2005, but this seems unlikely (Figure 24). The variables that went into the consideration of the 38 meter pumping depth by Ebraheem et al. (2003) are not specified. Perhaps this depth is factoring in the cost of new wells only. Therefore, the designation of uneconomic areas, particularly for 2020 and 2060, should be considered with this in mind. However, Figure 24 clearly shows a significant reduction in prospective drilling areas, particularly in the north. Only the southern area along the major north-south fault has potential for future groundwater development.

V.B. Conclusions

Multi-map analysis of several maps created from spaceborne remote sensing data and previously published work delineates potential sites for groundwater drilling in Egypt's Kharga Basin. This study has revealed:

- The Kharga is a closed basin that could have held water in the past.
- Thermal inertia values support the notion that the large north-south fault in the center of the Kharga Basin facilitates the vertical movement of water to the very near subsurface. However, this fault is not uniformly transmissive along its length.
- Fracture density did not have strong spatial correlation with higher thermal inertia values across the entire study area possibly due to the shallow depth at which this

parameter can be measured, but it should still be considered as a factor in determining future groundwater drilling sites.

- The southern end of the major north-south fault is the best possible location for shallow groundwater drilling.

REFERENCES

Abdel Zaher, M., N.M. Saadi, and K. Watanabeb (2014) Geological applications potential of DEM, ETM+, and gravity data in arid and semi-arid regions with special reference to south Western Desert, Egypt. Arabian Journal of Geosciences, 7, 1705-1716.

Abdelsalam, M.G., C. Robinson, F. El-Baz, and R.J. Stern (2000) Applications of orbital imaging radar for geologic studies in arid regions: The Saharan testimony. Photogrammetric Engineering and Remote Sensing, 66, 717-726.

Abdelsalam, M.G., J.P. Liegeois, and R.J. Stern (2002) The Saharan Metacraton. Journal of African Earth Sciences, 34, 119-136.

Abdelsalam, M.G., A.M. Youssef, S.M. Arafat, and M. Alfarhan (2008) Rise and demise of New Lakes of Sahara. Geosphere, 4, 375-386.

Abell, P.I. and P. Hoelzmann (2000) Holocene palaeoclimates in northwestern Sudan: Stable isotope studies on molluscs. Global Planetary Change, 26, 1-12.

Alaily, .F. and H.P. Blume (1993) Soil association and land suitability maps of the Western Desert, SW Egypt in: Meissner B. and P. Wycisk (eds.), Geopotential and Ecology: Analysis of a Desert Region. Catena Verlag, Cremlingen-Destedt. Germany.

Anudu, G.K., B.I. Essien, L.N. Onuba, and A.E. Ikpokonte (2011) Lineament analysis and interpretation for assessment of groundwater potential of Wamba and adjoining areas, Nasarawa State, northcentral Nigeria. Journal of Applied Technology in Environmental Sanitation, 1, 185-198.

Bastawesy, M.A., F. I. Khalaf, and S. M. Arafat (2008) The use of remote sensing and GIS for the estimation of water loss from Tushka lakes, southwestern desert, Egypt. Journal of African Earth Sciences, 52, 73-80.

Beyene, T., D.P. Lettenmaier, and P. Kabat (2010) Hydrologic impacts of climate change on the Nile River Basin: Implications of the 2007 IPCC scenarios. Climatic Change, 100, 33-461.

Boulos, F. K. (1990) Some aspects of the geophysical regime of Egypt in relation to heat flow, groundwater and microearthquakes in: Said, R. (ed.), The Geology of Egypt. A.A. Balkema, Rotterdam, Netherlands, 61-89.

Cai, G., Y. Xue, Y. Hu, Y. Wang, J, Guo, Y. Luo, C. Wu, S. Zhong, and S. Qi (2007) Soil moisture retrieval from MODIS data in Northern China Plain using thermal inertial model. International Journal of Remote Sensing, 28, 3567-3581.

Canadian Space Agency (2014) Radarsat-1, http://www.asc-csa.gc.ca/eng/satellites /radarsat1/default.asp (accessed March 29, 2016).

De Wit, M. and J. Stankiewicz (2006) Changes in surface water supply across Africa with predicted climate change. Science, 311, 1917-1921.

Djokic, D. (2008) Comprehensive Terrain Preprocessing Using Arc Hydro Tools, http://downloads2.esri.com/resources/datamodels/Comprehensive terrain preprocessing using Arc Hydro tools_2008.zip (accessed October 9, 2015).

Ebraheem, A.M., S. Riad, P. Wycisk, and A.M. Seif El Nasr (2002) Simulation of impact of present and future groundwater extraction from the non-replenished Nubian Sandstone Aquifer in southwest Egypt. Environmental Geology, 43, 188-196.

Ebraheem, A.M., H.K. Garamoon, S. Riad, P. Wycisk, and A.M. Seif El Nasr (2003) Numerical modeling of groundwater resource management options in the East Oweinat area, SW Egypt. Environmental Geology, 44, 433-447.

Ebraheem, A.M., S. Riad, P. Wycisk, and A.M. Sefelnasr (2004) A local scale groundwater flow model for groundwater resource management in Dakhla Oasis, SW Egypt. Hydrogeological Journal, 12, 714-722.

Embabi, N.S. (1982) Barchans of the Kharga Depression in: El-Baz, F. and T.A. Maxwell (eds.) Desert Landforms of Southwest Egypt: A Basis for Comparison with Mars. National Air and Space Museum Smithsonian Institution, Washington, DC, 141-155.

ESRI (2011) Arc Hydro Tools - Tutorial, http://downloads.esri.com/archydro/archydro/ Tutorial/Doc/Arc%20Hydro%20Tools%202.0%20-%20Tutorial.pdf (accessed October 7, 2015).

ESRI (2013) Overview of Arc Hydro Terrain Preprocessing Workflows, http://downloads.esri.com/archydro/archydro/Doc/Overview%20of%20Arc%20H ydro%20terrain%20preprocessing%20workflows.pdf (accessed October 7, 2015).

Ghoneim, E. and F. El-Baz (2007) DEM-optical-radar data integration for palaeohydrological mapping in the northern Darfur, Sudan: Implication for groundwater exploration. International Journal of Remote Sensing, 28, 5001-5018.

Gillespie, A.R. and A.B. Kahle (1977) Construction and interpretation of a digital thermal inertia image, Photogrammetric Engineering and Remote Sensing, 43, 983-1000.

Gossel, W. A.M. Ebraheem, and P. Wycisk (2004) A very large scale GIS-based groundwater flow model for the Nubian sandstone aquifer in Eastern Sahara (Egypt, northern Sudan, and eastern Libya). Hydrogeology Journal, 12, 698-713.

Haynes, C.V. (1982) The Darb El-Arba'in Desert: A Product of Quaternary Climatic Change. In: El-Baz, F. and T.A. Maxwell (eds.) Desert Landforms of Southwest Egypt: A Basis for Comparison with Mars. National Air and Space Museum Smithsonian Institution, Washington, DC, 91-117.

Heinl, M. and P.J. Brinkmann (1989) A groundwater model of the Nubian aquifer system. Hydrological Sciences Journal, 34, 425-447.

Hermina, M. (1990) The surroundings of Kharga, Dakhla, and Farafra Oases. In: Said, R. (ed.), The Geology of Egypt. A.A. Balkema, Rotterdam, Netherlands, 259-292.

Hesse, K.H, A. Hissene, O. Kheir, E. Schnacker, M. Schneider, and U. Thorweihe (1987) Hydrogeological investigations in the Nubian Aquifer system, Eastern Sahara. Berliner Geowiss-Abh (A), 75(2), 397-464.

Hoelzmann, P., H.J. Kruse, and F. Rottinger (2000) Precipitation estimates for the eastern Saharan palaeomonsoon based on water balance model of the West Nubian Palaeolake Basin. Global Planetary Change, 26, 105-120.

Kahle, A.B. (1977) A simple thermal model of the Earth's surface for geologic mapping by remote sensing, Journal of Geophysical Research, 82, 1673-1680.

Khan, S.D., M.S. Fathy, and M. Abdelazeem (2014) Remote sensing and geophysical investigations of Moghra Lake in the Qattara Depression, Western Desert, Egypt. Geomorphology, 207, 10-22.

Kieniewicz, J.M. and J.R. Smith (2007) Hydrologic and climatic implications of stable isotope and minor element analyses of authigenic calcite silts and gastropod shells from a mid-Pleistocene pluvial lake, Western Desert, Egypt. Quaternary Research, 68, 431-444.

Kieniewicz, J.M. and J.R. Smith (2009) Paleoenvironmental reconstruction and water balance of a mid-Pleistocene pluvial lake, Dakhleh Oasis, Egypt. Geological Society of America Bulletin, 121:7-8, 1154-1171.

Kropelin, S. (1993) Geomorphology, landscape evolution and paleoclimates of southwest Egypt. In: Meissner, B. and P. Wycisk (eds.), Geopotential and Ecology: Analysis of a Desert Region. Catena Verlag, Cremlingen-Destedt. Germany, 31-56.

Liang, S. (2000) Narrowband to broadband conversions of land surface albedo I: Algorithms, Remote Sensing of Environment, 76, 213-238.

Luo, W., R.E. Arvidson, M. Sultan, R. Becker, M.K. Crombie, N. Sturchio, and Z. El Alfy (1997) Ground-water sapping processes, Western Desert, Egypt. GSA Bulletin, 109, 43-62.

Ma, A.N. and Y. Xue (1990) A study of remote sensing information model of soil moisture. In Proceedings of the 11th Asian Conference on Remote Sensing, 15-21.

Mahmod, E.W., K. Watanabe, and A.A. Zahr-Eldeen (2013) Analysis of groundwater flow in arid areas with limited hydrogeological data using the Grey Model: A case study in the Nubian Sandstone, Kharga Oasis, Egypt. Hydrogeology Journal, 21, 1021-1034.

Maxwell, T.A., B. Issawi, and C.V. Haynes Jr. (2010) Evidence for Pleistocene lakes in the Tushka region, south Egypt. Geology, 38, 1135-1138.

McCauley, J.F., G.G. Schaber, C.S. Breed, M.J. Grolier, C. V. Haynes, B. Issawi, C. Elachi, and R. Blom (1982) Subsurface valleys and geoarcheology of the eastern Sahara revealed by shuttle radar. Science, 218, 1004-1020.

McHugh, W.P., J.F. McCauley, C.V. Haynes, C.S. Breed, and G.G. Schaber (1988) Paleorivers and geoarchaeology in the southern Egyptian Sahara. Geoarchaeology: An International Journal, 3, 1-40.

Meshref, W. M. (1990) Tectonic framework. In: Said, R. (ed.), The Geology of Egypt. A.A. Balkema, Rotterdam, Netherlands, 113-155.

Morgan, P. (1990) Egypt in the framework of global tectonics. In: Said, R. (ed.), The Geology of Egypt. A.A. Balkema, Rotterdam, Netherlands, 91-111.

NASA (2014) MODIS land team: Validation, Status for BRDF/Albedo (MCD43), http://landval.gsfc.nasa.gov/ (accessed September 3, 2015).

NASA (2016a) ASTER: Advanced Spaceborne Thermal Emission and Reflection Radiometer, http://asterweb.jpl.nasa.gov/ (accessed March 29, 2016).

NASA (2016b) Landsat Science: Operational Land Imager (OLI), http://landsat.gsfc.nasa.gov/?p=5447 (accessed March 29, 2016).

NASA (2016c) MODIS: Moderate Resolution Imaging Spectroradiometer, http://modis.gsfc.nasa.gov/ (accessed March 29, 2016).

NASA (2016d) Shuttle Radar Topography Mission: The Mission to Map the World, http://www2.jpl.nasa.gov/srtm/ (accessed March 29, 2016).

Pachur, H.J. and P. Hoelzmann (2000) Late Quaternary palaeoecology and palaeoclimates of the eastern Sahara. Journal of African Earth Sciences, 30, 929-939.

Pachur, H.J. and F. Rottinger (1997) Evidence for a large extended paleolake in the eastern Sahara as revealed by spaceborne radar lab images. Remote Sensing of the Environment, 61, 437-440.

Paillou, P., M. Schuster, S. Tooth, T. Farr, A. Rosenqvist, S. Lopez, and J. Malezieux (2009) Mapping of major paleodrainage system in eastern Libya using orbital imaging radar: the Kufrah River. Earth and Planetary Science Letters, 277, 327-333.

Peña, S.A and M.G. Abdelsalam (2006) Orbital remote sensing for geological mapping in southern Tunisia: Implication for oil and gas exploration. Journal of African Earth Sciences, 44, 203-219.

Pratt, D.A. and C.D. Ellyett (1979) The thermal inertia approach to mapping of soil moisture and geology. Remote Sensing of Environment, 8, 151-168.

Price, J.C. (1985) On the analysis of thermal infrared imagery: The limited utility of apparent thermal inertia, Remote Sensing of Environment, 18, 59-73.

Quinn, J.W. (2001) Band combinations, Portland State University, http://web/pdx.edu/emch/ip1/bandcombinations.html (accessed November 4, 2015).

Robinson, C.A. (2002) Application of satellite radar data suggest that the Kharga Depression in south-western Egypt is a fracture rock aquifer. International Journal of Remote Sensing, 23, 4101-4113.

Robinson, C.A., A. Werwer, F. El-Baz, M. El-Shazly, T. Fritch, and T. Kusky (2007) The Nubian Aquifer in southwest Egypt. Hydrogeology Journal, 15, 33-45.

Said, R. (1990) Geomorphology. In: Said, R. (ed.), The Geology of Egypt. A.A. Balkema, Rotterdam, Netherlands, 9-25.

Scheidt, S., M. Ramsey, and N. Lancaster (2010) Determining soil moisture and sediment availability at White Sands Dune Field, New Mexico, from apparent thermal inertia data. Journal of Geophysical Research, 115, F02019, doi: 10.1029/2009JF001378.

Senosy, M.M., M.M. Youssef, and M. Abdel Zaher (2013) Sedimentary cover in the South Western Desert of Egypt as deduced from Bouguer gravity and drill-hole data. Journal of African Earth Sciences, 82, 1-14.

Smith, J.R., R. Giegengack, and H.P. Schwarcz (2004a) Constraints on Pleistocene pluvial climates through stable-isotope analysis of fossil-spring tufas and associated gastropods, Kharga Oasis, Egypt. Palaeogeography, Palaeoclimatology, Palaeoecology, 206, 157-175.

Smith, J.R., R. Giegengack, H.P. Schwarcz, M.M.A McDonald, M.R. Kleindienst, A.L. Hawkins, and C.S. Churcher (2004b) A reconstruction of Quaternary pluvial environments and human occupations using stratigraphy and geochronology of fossil-spring tufas, Kharga Oasis, Egypt. Geoarchaeology: An International Journal, 19, 407-439.

Smith, J.R., A.L. Hawkins, Y. Asmerom, V. Polyak, and R. Giegengack (2007) New age constraints on the Middle Stone Age occupations of Kharga Oasis, Western Desert, Egypt. Journal of Human Evolution, 52, 690-701.

Szabo, B.J., C.V. Haynes, and T.A. Maxwell (1995) Ages of Quaternary pluvial episodes determined by uranium-series and radiocarbon dating of lacustrine deposits of Eastern Sahara. Palaeogeography, Palaeoclimatology, Palaeoecology, 113, 227-242.

Tewksbury, B.J., E.A. Tarabees, J.P. Hogan, S.A. Kattenhorn, and C. Mehrtens,(2013) The Desert Eyes Project part I; polygonal faults in Cretaceous chalk and enigmatic fold structures in Eocene limestones, Western Desert, Egypt. Abstracts with Programs - Geological Society of America, 45, 7, 160.

The Weather Channel LLC (2015) Weather Underground: Historical Weather, www.wunderground.com/history/ (accessed September 21, 2015).

Thorweihe, U. (1990) Nubian Aquifer system. In: Said, R. (ed.), The Geology of Egypt. A.A. Balkema, Rotterdam, Netherlands, 601-611.

Thorweihe, U. and M. Heinl (1993) Hydrogeology in: Meissner, B. and P. Wycisk (eds.), Geopotential and Ecology: Analysis of a Desert Region. Catena Verlag, Cremlingen-Destedt. Germany.

U.S. Department of the Interior, U.S. Geological Survey (2008) Shuttle Radar Topography Mission, http://srtm.usgs.gov/mission.php (accessed October 13, 2015).

U.S. Department of the Interior, U.S. Geological Survey (2014) LP DAAC MODIS/Aqua Land Surface Temperature and Emissivity 5-minute L2 Swath 1 km, https://lpdaac.usgs.gov (accessed September 3, 2015).

Wan, Z. (1999) MODIS land-surface temperature algorithm theoretical basis document (LST ATBD). Institute for Computational Earth System Science, Santa Barbara, 75.

Wan, Z., Y. Zhang, Q. Zhang, and Z.-L. Li (2004) Quality assessment and validation of the MODIS global land surface temperature, International Journal of Remote Sensing, 25, 261-274.

Wetzel, P.J., D. Atlas, and R.H. Woodward (1984) Determining soil moisture from geosynchronous satellite infrared data: A feasibility study, Journal of Climate and Applied Meteorology, 23, 375-391.

Xue, Y. and A.P. Cracknell (1995) Advanced thermal inertia modelling, International Journal of Remote Sensing, 16, 431-446.

Zakey, A.S., M.M. Abdelwahab, and P.A. Makar (2004) Atmospheric turbidity over Egypt. Atmospheric Environment - Africa and the Middle East, 38, 1579-1591.

Zhang, R., X. Sun, Z. Zhu, H. Su, and X. Tang (2003) A remote sensing model for monitoring soil evaporation based on differential thermal inertia and its validation, Science in China D, 46, 342-355.

APPENDICES

Appendix A

Thermal Inertia: Atmospheric Transmittance Calculation

Thermal inertia studies commonly assume the atmospheric transmittance to be 0.75 (Xue and Cracknell 1995; Cai et al. 2007; Scheidt et al. 2010). Atmospheric transmittance is a ratio of transmitted electromagnetic energy to total electromagnetic energy. The atmospheric transmittances for this study were calculated from the Beer's Lambert Law:

$$T = e^{-\tau} \tag{13}$$

T = transmittance

τ = aerosol optical depth

This value is then divided by one to find the percentage of radiation transmitted. The aerosol optical depths used were average monthly values calculated from 1989-1995 over Aswan, Egypt, which is about 280 km to the southeast of Kharga, Egypt (Zakey et al. 2004). Furthermore, aerosol optical thickness by specific month of the dates in this study was obtained from the NASA Earth Observations website: http://neo.sci.gsfc.nasa.gov.

This website has color charts of the aerosol optical depths but not exact values. The color charts over Kharga Basin were in keeping with the values obtained by Zakey et al. (2004) over Aswan. The calculated transmittance ratios were very near the standard value used by other researchers (Table 3).

Table 3. Atmospheric transmittance ratios (C_t).

Month	C_t
March	0.74
April	0.73
May	0.72
June	0.73

Appendix B

The TI images for the three datasets not provided in Figures 12-13 are provided in Figure 28. They show values slightly higher than the 2010 data but remain relatively the same. Because of the larger ΔT for the 2010 data set, the lower wind speeds, and the smaller range in winds speeds throughout the day the values for the 2010 dataset are likely to be most accurate. All four images are quite equivalent in a relative sense as the oasis areas, the dune belt running north-south in the center, and the areas of higher TI values in the west are all similar. The 2015 data set has the lowest mean albedo of the four, and this is most likely the cause of the overall higher TI values. The higher TI values in the SW corner of the study area just north of the plateau edge is another area with a lithological change that can be seen in Landsat images results in subsequently higher TI values. These images highlight the fact that although the thermal inertia model gives consistent thermal inertia values, slight changes in measured and unmeasured

variables can limit accuracy. However, the results are consistent with the oases having

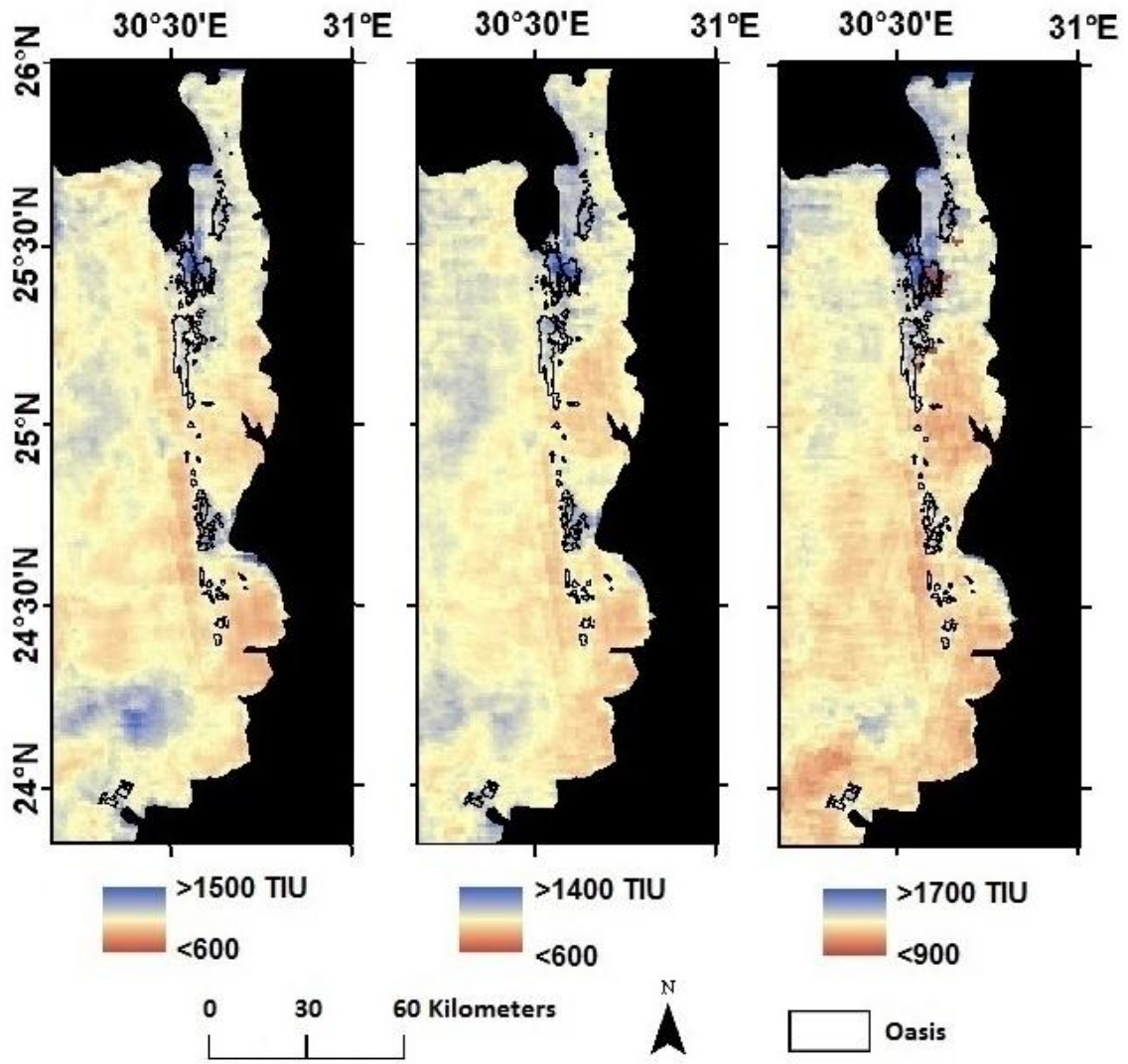soil moisture high enough to support vibrant plant life.

Figure 28: Kharga Basin thermal inertia derived from a) March 2013, b) April 2013, and
c) June 2015 data.

VITA

Shawna Lee Parks

Candidate for the Degree of

Master of Science

Thesis: REMOTE SENSING ANALYSIS AND IMPLICATIONS FOR GROUNDWATER RESOURCES IN THE KHARGA BASIN, EGYPT

Major Field: Geology

Biographical:

Education:

Completed the requirements for the Master of Sciences in geology at Oklahoma State University, Stillwater, Oklahoma in May 2016.

Completed the requirements for the Bachelor of Arts in journalism at the University of Central Oklahoma, Edmond, Oklahoma in 2004.

Experience:

Geophysics internship with Devon Energy in summer 2015.

Professional Memberships:

Society of Exploration Geophysicists (SEG)
American Association of Petroleum Geologists (AAPG)